Deletion of Mocos induces xanthinuria with obstructive nephropathy and major metabolic disorders in mice

Delphine Sedda, Claire Mackowiak, Julie Pailloux, Elodie Culerier, Ana Dudas, Pauline Rontani, Nicolas Erard, Antoine Lefevre, Sylvie Mavel, Patrick Emond, et al.

Kidney360 Publish Ahead of Print, published on September 17, 2021 as doi:10.34067/KID.0001732021

Kidney360

American Society of Nephrology
1401 H St NW, Suite 900
Washington, DC 20005
Phone: 202-640-4660 | Fax 202-637-9793
vramsey@kidney360.org

Article Type: Original Investigation

Deletion of *Mocos* induces xanthinuria with obstructive nephropathy and major metabolic disorders in mice

DOI: 10.34067/KID.0001732021

Delphine Sedda, Claire Mackowiak, Julie Pailloux, Elodie Culerier, Ana Dudas, Pauline Rontani, Nicolas Erard, Antoine Lefevre, Sylvie Mavel, Patrick Emond, Frederic Foucher, Marc Le Bert, Valerie Quesniaux, Michael Mihatsch, Bernhard Ryffel, and Madeleine Erard-Garcia

Key Points:
*A knockout mouse targeting the molybdenum cofactor sulfurase (*Mocos*) gene develops xanthinuria type II with lethal obstructive nephropathy

*Xanthinuric *Mocos* KO mice display moderate renal inflammation and fibrosis, normocytic anemia and reduced detoxification defense systems

*Purine, but also amino acids and phospholipids metabolic pathways are altered in *Mocos* knockout kidneys

Abstract:
Background: Xanthinuria type II is a rare autosomal purine disorder. This recessive defect of purine metabolism remains an underrecognized disorder. Methods: Mice with targeted disruption of the molybdenum cofactor sulfurase (Mocos) gene were generated to enable an integrated understanding of purine disorders and evaluate pathophysiological functions of this gene found in large number of pathways and known to be associated with autism. Results: Mocos deficient mice die with 4 weeks of age due to renal failure of distinct obstructive nephropathy with xanthinuria, xanthine deposits, cystic tublular dilatation, Tamm Horsfall (uromodulin) protein deposits, tubular cell necrosis with neutrophils and occasionally hypdronephrosis with urolithiasis. Obstructive nephropathy is associated with moderate interstitial inflammatory and fibrotic responses, anemia, reduced detoxification systems and important alterations of the metabolism of purines, amino acids and phospholipids.Conversely, heterozygous mice expressing reduced MOCOS protein are healthy with no apparent pathology. Conclusions: Mocos deficient mice develop a lethal obstructive nephropathy associated with profound metabolic changes. Studying MOCOS functions may provide important clues about the underlying pathogenesis of xanthinuria and other diseases requiring early diagnosis

Disclosures: All authors have nothing to disclose.

Funding: FEDER:, EX005756 =BIO-TARGETII N{degree sign}2016-00110366=BIO-TARGET 2015-2018

Author Contributions: Delphine Sedda: Conceptualization; Investigation Claire Mackowiak: Conceptualization; Data curation; Formal analysis; Investigation Julie Pailloux: Conceptualization; Investigation Elodie Culerier: Conceptualization Ana Dudas: Investigation Pauline Rontani: Conceptualization; Investigation Nicolas Erard: Investigation Antoine Lefevre: Conceptualization Sylvie Mavel: Conceptualization; Data curation; Formal analysis Patrick Emond: Data curation; Formal analysis Frederic Foucher: Conceptualization; Data curation Marc Le Bert: Conceptualization Valerie Quesniaux: Project administration Michael Mihatsch: Conceptualization; Data curation; Formal analysis; Investigation; Writing - original draft; Writing - review and editing Bernhard Ryffel: Funding acquisition Madeleine Erard-Garcia: Conceptualization; Data curation; Investigation; Project administration; Supervision; Validation; Writing - original draft; Writing - review and editing

Clinical Trials Registration: No

Registration Number:

Registration Date:

How to Cite this article: Delphine Sedda, Claire Mackowiak, Julie Pailloux, Elodie Culerier, Ana Dudas, Pauline Rontani, Nicolas Erard, Antoine Lefevre, Sylvie Mavel, Patrick Emond, Frederic Foucher, Marc Le Bert, Valerie Quesniaux, Michael Mihatsch, Bernhard Ryffel, and Madeleine Erard-Garcia, Deletion of *Mocos* induces xanthinuria with obstructive nephropathy and major metabolic disorders in mice, Kidney360, Publish Ahead of Print, 10.34067/KID.0001732021

Deletion of *Mocos* induces xanthinuria with obstructive nephropathy and major metabolic disorders in mice

Delphine Sedda[1], Claire Mackowiak[1], Julie Pailloux[1], Elodie Culerier[1], Ana Dudas[1], Pauline Rontani[2], Nicolas Erard[2], Antoine Lefevre[3], Sylvie Mavel[3], Patrick Emond[3,4,5], Frederic Foucher[6], Marc Le Bert[1], Valerie FJ Quesniaux[1], Michael J. Mihatsch[7], Bernhard Ryffel[1] and Madeleine Erard-Garcia[1]

[1]Experimental and Molecular Immunology and Neurogenetics (INEM), Orleans University, CNRS UMR7355, Orleans, France.
[2]Institut of NeuroPhysiopathology (INP), Aix-Marseille University, CNRS UMR7051, Marseille, France.
[3]iBrain, Tours University, Inserm UMR 1253, Tours, France.
[4]Division of In Vitro Nuclear Medecine, Regional University Hospital of Tours, France.
[5]PST Analysis of Biological Systems, Tours University, France.
[6]Center for Molecular Biophysics (CBM), CNRS UPR4301, Orléans, France.
[7]Institute for Pathology, University Hospital of Basel, Basel, Switzerland.

Correspondence to :
Madeleine Erard-Garcia
CNRS - UMR 7355 - INEM
3B, rue de la Férollerie
45071 Orléans cedex 2
FRANCE
Tél: +33 2 38 25 79 70
E-mail madeleine.erard@cnrs-orleans.fr

Key points

- A knockout mouse targeting the molybdenum cofactor sulfurase (*Mocos*) gene develops xanthinuria type II with lethal obstructive nephropathy.
- Xanthinuric *Mocos* KO mice display moderate renal inflammation and fibrosis, normocytic anemia and reduced detoxification defense systems.
- Purine, but also amino acids and phospholipids metabolic pathways are altered in *Mocos* knockout kidneys.

Abstract

Background: Xanthinuria type II is a rare autosomal purine disorder. This recessive defect of purine metabolism remains an underrecognized disorder.

Methods: Mice with targeted disruption of the molybdenum cofactor sulfurase (*Mocos)* gene were generated to enable an integrated understanding of purine disorders and evaluate pathophysiological functions of this gene found in large number of pathways and known to be associated with autism.

Results: *Mocos* deficient mice die with 4 weeks of age due to renal failure of distinct obstructive nephropathy with xanthinuria, xanthine deposits, cystic tubular dilatation, Tamm Horsfall (uromodulin) protein deposits, tubular cell necrosis with neutrophils and occasionally hypdronephrosis with urolithiasis. Obstructive nephropathy is associated with moderate interstitial inflammatory and fibrotic responses, anemia, reduced detoxification systems and important alterations of the metabolism of purines, amino acids and phospholipids.Conversely, heterozygous mice expressing reduced MOCOS protein are healthy with no apparent pathology.

Conclusions: *Mocos* deficient mice develop a lethal obstructive nephropathy associated with profound metabolic changes. Studying MOCOS functions may provide important clues about the underlying pathogenesis of xanthinuria and other diseases requiring early diagnosis

Introduction

Xanthinuria is rare hereditary disorder of purine metabolism. Two forms can be distinguished: namely classic xanthinuria type I, caused by xanthine dehydrogenase (XDH) deficiency alone and xanthinuria type II, caused by the dual deficiency of XDH and aldehyde oxidase1 (AOX1), two enzymes whose activity depends on the presence of molybdenum cofactor sulfurase (MOCOS). Both forms are autosomal recessive disorders displaying identical clinical phenotypes. In about two-thirds of affected individuals, xanthinuria remains an asymptomatic metabolic abnormality throughout life. In the remaining one-third, xanthine stones form and lead to varying degrees of nephrolithiasis, hydronephrosis, and, in some cases, renal failure[1]. Clinically, both forms are characterized by marked depletion of uric acid, accumulation of xanthine in blood and urine. Other less common manifestations linked to xanthine deposits may develop such as myositis, arthropathy and duodenal ulcer[2]. The differential diagnosis between type I and type II classical xanthinuria relies on a detailed medical history and allopurinol response in hypouremic patients with xanthinuric type II patients failing to metabolize allopurinol into oxypurinol[3].

To date, the true incidence and prevalence of classic xanthinuria is not known because it is rarely reported and often not recognized and underexplored. In this context, only few cases of xanthinuria type II caused by point mutations in the coding sequence of *MOCOS* have been reported in human[4-9]. *MOCOS* encodes a ubiquitous enzyme that catalyzes the insertion of a terminal sulfur ligand onto MOCO, the molybdenum cofactor, converting the oxo form of MOCO into a sulfurated form[10]. The structure of the mammalian MOCOS is similar to ABA3, its plant homologue: it is a two-domain protein containing an N-terminal domain showing homologies to L-cysteine desulfurase and a C-terminal domain able to bind the molybdenum cofactor MOCO[11-13]. After sulfuration by MOCOS, sulfurated-MOCO is required to activate XDH and AOX1, two structurally complex oxidoreductases. XDH is a rate-limiting enzyme in

the oxidative metabolism of purines: it allows the conversion of hypoxanthine and xanthine to uric acid as well as the oxidation of allopurinol to oxypurinol[14]. XDH is thought to play a key role in a variety of physiological but also pathophysiological conditions such as ischemia–reperfusion injury, endothelial dysfunction, diabetes mellitus but also cardiovascular diseases, renal failure and cancer[15]. It is also a significant component of innate inflammatory signaling and a major source of reactive oxygen species (ROS)[16]. Conversely, little is known about the physiological relevance of AOX1, except that it catalyzes the oxidation of several aldehydes to their cognate acids[17]. As XDH, AOX1 is a critical source of ROS and nitric oxide (NO) and it is increasingly recognized as a major contributing factor to drug metabolism and as a source of ROS possibly involved in human pathology[18, 19].

No study on the potential impact of *MOCOS* deletion on kidney function and the mechanism by which such mutation could contribute to xanthinuria have been performed. In addition, *MOCOS* alterations may cause genetic damage of their own and orchestrate a wide variety of clinical syndromes. MOCOS deficiency might be regarded as a risk factor in autism spectrum disorders (ASD), disrupting oxidative stress response and synaptogenesis in neurons derived from human induced-pluripotent stem cells[20-22]. While these results indicate that *MOCOS* serves important functions in tissue homeostasis and during neuronal development, the reasons for the wide range of pathophysiological phenotypes observed in *MOCOS* deficiencies are unclear. To gain insights into the role of MOCOS in purine metabolism and yet unidentified pathways, we have analyzed a new mouse model knockout for *Mocos*.

We show here that *Mocos* KO mice die within 4 weeks with xanthinuria and renal failure. While heterozygous *Mocos* mice grow normally into apparently healthy fertile adults, *Mocos* KO mice develop obstructive nephropathy with xanthine deposits. In xanthinuric mice, reduced antioxidant defense systems along with anemia may also be involved in the progression of renal injury. Finally, consistent with a role of MOCOS in various signaling pathways, we also report

major differences of metabolism between kidneys of *Mocos* KO and littermate wild type mice, which are related to purine but also amino acids and phospholipids metabolic pathways. These observations suggest that, in addition to its role in purine metabolism leading to obstructive nephropathy, MOCOS deficiency unveils yet unknown functions in other metabolic processes.

Methods

Generation of Mocos$^{em2(IMPC)Ics}$ knockout mice and animal matings

The CRISPR/Cas9 system was used to generate mice with complete *Mocos* knockout by zygotic injection of CAS9 and multiple adjacent single-guide RNAs (sgRNAs) that target exon 3. Genome editing was performed at PHENOMIN-Mouse Clinical Institute (ICS, Strasbourg-France). The conditions used at ICS to generate the *Mocos* KO via CRISPR/Cas9 approach, can be found in the ICS website (http://www.ics-mci.fr/).

PHENOMIN projects has received an approval from ethic committees and an authorization from the Ministry of Research (France). Project evaluation was realized following the 3Rs and HBA concepts with a huge attention on refinement (use of anesthesia, of painkillers when needed, respect of good practices).

Specific primer sequences used for genotyping were as follow:

Mocos For: GGGGATTGTTGTATTGTGCCTGTCTG

Mocos Rev: CTTGCCCTCTGTCTTCTGACCTGAGG.

Mocos KO mice were obtained by crossing heterozygous mice for the gene *Mocos*. Experiments were performed with 4 to 10 week-old female or male mice. All *Mocos*-deficient mice and WT littermate controls (C57BL/6J background) were bred and housed in our specific pathogen-free animal facility at TAAM (Transgenesis, Archiving and Animal Models, TAAM-UPS 44, CNRS, Orleans, France) under agreement D-45-234-6, 2014. Mice were maintained in a temperature-controlled (23°C) facility with strict 12-hour light/dark cycles and given free access to food and water. Animal experiments were performed according to the French Institutional Committee under agreement CLE CCO 2017-1134.

Hematology and urine analysis

Blood was collected in EDTA tubes (Sarstedt 20.1341.100) and read with analyzer SCIL vet abc+. Before use, serum was collected in microvette gel tubes (Sarstedt 20.1344) and centrifuge 10000g for 5 min. The Xanthine/Hypoxanthine levels were determined using the Xanthine/Hypoxanthine Assay kit (Abcam, ab155900) following manufacturer's protocol. Urine was freshly collected and pH was determined with pH indicator paper (Whatman, 2600 108).

Histological and Immunofluorescence Analysis

Dissected tissues were fixed in 4% buffered paraformaldehyde and paraffin embedded under standard conditions. Tissue sections (3µm) were stained with hematoxylin–eosin (HE) and special stains according to standard laboratory procedures. Immunohistochemistry for uromodulin/Tamm Horsfall Protein was performed according to standard procedures (https://esp-nephropathology-working-group.org/technical-notes/) with a mouse monoclonal antibody purchased from Cedarlane.

For Immunofluorescence, tissues were fixed for 3 days in 4% PFA and submerged in 20% sucrose for 1 week. They were then embedded in OCT (Tissue-Teck) and 10 µM sections were prepared with cryotome (Leica). TUNEL staining was performed on sections using the ApopTag® Fluorescein In Situ Apoptosis Detection kit (Merck, S7110) following manufacturer's protocol. For Ki67 (PCNA) staining, slides were incubated 30 min in citrate buffer at 80 °C, washed in TBS-Tween and then incubated overnight with rabbit-anti-mouse-Ki67 (Abcam, 4 µg/ml, ab15580). After washing slides were treated with 0,05% pontamin sky blue (Sigma) for 15 min and then incubated with secondary goat anti-rabbit antibody (Abcam ,2µg/mL, ab150077) for 45 min at room temperature. After washing, slides were incubated with DAPI (Fisher Scientific) and mounted in fluoromount® (SouthernBiotech). Tissue sections

were analysed on a Leicafluorescence microscope Leica (Leica, CTR6000) at x200 magnification. The slides were analyzed and semi-quantitatively scored.

RNA preparation, PCR and qPCR

Total RNA was extracted using TRI-Reagent (Sigma) according to the manufacturer's instruction. RNA integrity and quality were controlled using Agilent RNA 6000 Nanopuces kit®. Reverse transcription was performed with SuperScript®III Kit (Invitrogen), and the resultant cDNAs were quantitatively amplified with real-time-PCR using QuantiTect® Primer Assay kit (Qiagen) and GoTaq® qPCR-Master Mix (Promega). RNA expression was normalized to TBP (TATA-Binding Protein) expression and data were analyzed using the comparative analysis of relative expression by $^{\Delta\Delta}$Ct methods. Primers sequences are reported in Supplemental Table 1.

Western blot

Protein concentrations were quantified using the Bio-Rad DC™ protein assay kit following manufacturer's instructions. After blocking, membranes were probed with rabbit anti-MOCOS (Novus biologicals, NBP2-14243, 1/100), rabbit anti AKR1C1 (GeneTex 105620, 1/1000) or mouse anti-β-Actin (Sigma-Aldrich, A2228, 1/5000) antibodies. After overnight incubation at 4°C, the appropriate horseradish peroxidase-conjugated secondary IgG antibodies were added for 2 hours at room temperature. Signals were quantified using ImageJ software.

Metabolic analysis

Metabolic analyses were performed by liquid chromatography coupled with high resolution mass spectrometry (LC-HRMS) based on standard metabolomics approaches[23, 24]. Briefly, frozen kidney tissue samples were lyophilized during 48 h and milled to a fine powder. Two

milligrams of ground samples were extracted with 1.5 mL of Methanol/milliQ water (1/1). After centrifugation, the supernatants were collected and concentrated at 35°C for 2h30. the analyses were done on a UPLC Ultimate 3000 system (Dionex), coupled to a Q-Exactive mass spectrometer (Thermo Fisher Scientific, Germany) and operated in positive (ESI+) and negative (ESI−)electro spray ionization modes. Chromatography was carried out with a PhenomenexKinetex1.7mXB C18 (150mm×2.10mm) and 100Å UHPLC column. The solvent system comprised mobile phase A [0.1% (vol/vol) formic acid in water], and mobile phase. Data were processed using Xcalibur® software (Thermo Fisher Scientific, San Jose, CA). A library of standard compounds (Mass Spectroscopy Metabolite Library of Standards MSMLS supplied by IROA TechnologiesTM) were analyzed with the same conditions and gradient of mobile phases than those used to analyze the extracted metabolites. For data processing, briefly, peaks with greater than 30% variance (CV %) in quality control samples were removed. The normalization was done to the total area of the peaks of interest. The multivariate analyses were done using Simca-P+-15 software (Umetrics, Umeå, Sweden) as previously described[25]. Briefly, the data analyses were first conducted using principal component analysis (PCA) to detect outliers. Discriminant metabolites were obtained after orthogonal partial least squares discriminant analysis (OPLS-DA), after elimination of metabolites with low impact in the separation of the different groups. The listing of discriminant metabolites [very important in projection (VIP)] is given in supplemental Table 2. Univariate analyses were performed as non-parametric tests (Wilcoxon rank-sum test) using the web free server Metaboanalyst[52] (https://www.metaboanalyst.ca/) with an FDR adjusted p-value of 0.05.

Statistical analysis

All values were presented in the form of mean±SEM. Statistical evaluation of differences between the experimental groups was done by Mann-Whitney non-parametric test, or Log Rank

test for survival. All tests were performed with GraphPad Prism [GraphPad Software Inc., San Diego, CA, USA; www.graphpad.com]. A *P*-value <0.05 was considered significant and symbolized with *; ** for *P*<0.01 and *** for *P*<0.001.

Results

Mice containing a null mutation of *Mocos* induces a partial lethal phenotype and die prematurely

To characterize the physiological role of *Mocos*, mice with a targeted disruption in the *Mocos* locus were generated using CRISPR/Cas9 genome editing technology (Figure 1A). After validation of the deletion by sequencing, a significant reduction of *Mocos* mRNA and MOCOS protein levels further confirmed targeting of the gene in engineered mice. Transcript level and protein concentration were reduced to roughly half in heterozygous *Mocos*$^{+/-}$mice (Figure 1B and C).

Mice homozygous for the disrupted Mocos gene were born phenotypically normal (Figure 1D) but only few mice were recovered at weaning, pointing toward late embryonic or perinatal lethality. Further analysis showed that there was an increased frequency of dead pups after birth although the exact frequency cannot be determined due to cannibalization by the mother. These findings indicate a high perinatal mortality of homozygous pups. Young *Mocos*$^{-/-}$mice were easily recognized from littermate controls after the first two weeks of life when they stopped gaining weight (Figure 1E, F). Shortly after, all *Mocos* KO mice died between 3 to 8 weeks of age with an average lifespan of 28,4 days (Figure 1G, H). In contrast, heterozygous mice were not different from wild type mice derived from heterozygous breeding pairs; the mice survived and developed normally into apparently healthy fertile adults (Supplemental Figure 1A). These observations indicated that *Mocos* deficiency in mouse leads to a lethal

phenotype with incomplete penetrance and premature death. Because of the runted appearance of the *Mocos* KO mice, all subsequent analyses were conducted on *Mocos* KO mice before death between 3 and 4 weeks of age. In addition, a close monitoring of heterozygous mice for possible signs of disease was prolonged in adult animals ranging from 2 to 20 months of age.

Inactivation of *Mocos* causes abnormal morphological features

At 4 weeks of age, *Mocos* deficient mice displayed major morphologic abnormalities with significant reductions in kidney/ and liver/body weight ratios (33% and 20% reduction respectively) and a substantial increase in brain/body weight ratios (51% increase) when compared to organ/body weight sizes of littermate controls (Supplemental Figure 1B-E). No significant differences in the size or gross morphology in all other organs including lung, spleen or intestine were observed (Supplemental Figure 1F-H). In contrast, *Mocos* heterozygotes showed normal proportions of all organs except the liver which showed a 21% reduction in liver/body weight size when compared to young wild type mice (Supplemental Figure 1B-H).

Mocos KO mice develop obstructive nephropathy

Anatomical examination of *Mocos*$^{-/-}$ mice revealed that all internal organs appeared grossly normal with the exception of the kidneys. Macroscopically, the mutation produces profound modifications of the renal structure: kidneys were pale, reduced in size with an irregular surface, while heterozygous *Mocos*$^{+/-}$ mice and wild type littermates appeared normal (Supplemental Figure 1B-C). At low power magnification, the histological evaluation of *Mocos* KO kidneys displayed three major lesions: i) cystic dilatation of tubules mainly in the cortex and less in the medulla (Figure 2A), ii) intra-tubular deposits of round lamellate deposits of Tamm-Horsfall protein with occasionally embedded crystals (empty crystal clefts, Figure 2C-D) and iii) Tamm Horsfall protein deposits in the renal pelvis with damage of the urothelium,

accompanied by inflammation in the surrounding tissue. In the dilated and non-dilated collecting ducts, round lamellate deposits of Tamm-Horsfall protein are present (Figure 2C). These deposits often display a basophilic rim - suggestive of calcification - but give a negative Kossa staining and no birefringent crystals are found after paraformaldehyde fixation. Few empty crystal clefts are, however, present (Figure 2C). The adjacent epithelium is flattened or necrotic with intraluminal cell debris shed with neutrophils and a few multinucleated giant cells are surrounding the deposits (Figure 2C). The interstitial space is slightly oedematous and, adjacent to dilated collecting ducts, cortical areas display tubular atrophy, interstitial fibrosis and mononuclear cell infiltrates (predominately in the subcapsular area) (Figure 2B-D). Primary lesions in glomeruli and vessels are not found. In areas of tubular atrophy, the glomeruli lie close together, vary in size, have collapsed capillary loops and are very rarely sclerotic. Moreover, some deposits of Tamm Horsfall protein, similar to those present in the collecting ducts, are also found in the renal pelvis. These deposits are adhering to the urothelium, giving rise to urothelial damage and loss. Outside the renal pelvis inflammatory infiltrates are seen (Figure 2D).

Occasionally, in about 5% of *Mocos* KO mice, stones are found in the pelvis and may lead to ureteral obstruction. This obstruction was mostly unilateral and kidneys were displaying a pale and swollen appearance. The histological examination of these enlarged kidneys showed a uniformly thin atrophic renal cortex and a marked dilation of the renal pelvis, characteristic of hydronephrosis (Supplemental Figure 2), while the contra-lateral kidney was small with obstructive nephropathy. Of note, heterozygous mice with partial loss of *Mocos* expression did not disturb the histology of other organs in young mice or later in adult mice (Supplemental Figure 3).

Inactivation of *Mocos* induces xanthinuria

Because stones sometimes clearly visible to the naked eye and large enough to interfere with normal urinary function were frequently observed in urine and kidneys from affected *Mocos* mice (Figure 3A), we next analyzed the effects of urinary tract obstruction in biological fluids. Consistent with a role of *Mocos* in purine metabolism, the colorless and acidic urine (Figure 3B), but also the serum collected from *Mocos*$^{-/-}$ mice had high levels of xanthine and hypoxanthine as compared with age-matched controls (Figure 3C, D). Kidney stones were composed of xanthine based on their unique Raman spectral fingerprints (Figure 3E, F). The present morphological and biochemical data thus strongly suggest that accumulation of xanthine crystals leads to intra- and extra-renal obstructive nephropathy in *Mocos* KO mice. Xanthine stones with hydronephrosis are found in mice as well as in hereditary xanthinuria type II in human which is typical crystallopathy, but the prevailing feature in the *Mocos* KO mouse model is an obstructive nephropathy.

Renal failure *in Mocos* KO mice

Kidney dysfunction in *Mocos* deficient mice was further evaluated by monitoring biochemical markers for the diagnosis of the progression of kidney damage. Our data denote profound metabolic changes, including drastic increases of serum creatinine and urea in *Mocos*$^{-/-}$mice when compared to controls (Figure 4A, B). As expected from the essential role of *Mocos* in XDH activity, *Mocos* KO mice had an almost undetectable level of uric acid (Figure 4C). In addition, the serum levels of some hepatic enzymes were altered with a reduced level of alanine aminotransferase (ALAT) and an increased level of alkaline phosphatase (ALP) in *Mocos* deficient mice (Figure 4D-F), which were not observed in heterozygous *Mocos* animals when compared to wild type mice at 4 weeks of age or later in adult mice (Supplemental Figure 4A-F). Altogether, these data suggested that the physiopathological changes produced by the complete inactivation of *Mocos* caused acute renal failure.

Mocos KO mice display anemia

Because hematological parameters are tightly regulated traits with high clinical relevance, we also analyzed the haematogram of *Mocos*$^{-/-}$ and control mice. When compared to littermate controls, *Mocos* KO mice tend to have almost normal distribution of total white blood cells (WBC) counts (Figure 5). The differential cell counts to identify leukocytes were within the normal range as was the number of platelet. This result excluded a systemic inflammation but it also underscored the presence of mild anemia with reduced circulating red blood cells (RBC) and red cell parameters values outside normal ranges. Of note, hemoglobin and hematocrit values in *Mocos*$^{-/-}$ mice were significantly decreased compared with that in wild type mice (Figure 5). These disturbances, accompanied by normal values of mean corpuscular volume and mean corpuscular hemoglobin concentration were suggestive of normocytic anemia, a feature frequently associated with poor outcomes in acute and chronic renal failure[26]. On the contrary, heterozygous *Mocos* mice showed normal haematological parameters at 4 weeks of age and even later (Supplemental Figure 5).

Mocos KO mice display increased expression of adipogenesis-related genes, and markers of inflammation and fibrosis

We further investigated dysregulation of lipid metabolism and found enhanced expression of two important regulators of lipid homeostasis, namely CCAAT/enhancer-binding protein-β (C/EBP-β) and peroxisome proliferator activated receptorγ (PPARγ) in *Mocos* KO mice compared with age-matched counterparts (Figure 6A). This altered lipid signaling network could contribute to the pathophysiology of xanthinuria and interfere with immune regulation because we observed a marked increase in mRNA expression of the proinflammatory factors tumor necrosis factor α (TNF-α) and monocyte chemoattractant protein1 (MCP1/CCL2)

(Figure 6B). Finally, the significant activation of transforming growth factor β1 (TGFβ1), may contribute to renal interstitial fibrosis [27, 28], and serpine 1, the main suppressor of the fibrinolytic system, suggesting a vicious cycle of immune-metabolic dysregulation could promote renal fibrotic responses and kidney dysfunction in *Mocos*$^{-/-}$ kidneys (Figure 6C). Immunofluorescence imaging ultimately supported visual evidence for tubular damage and repair with increased Apoptag staining (Figure 6D) accompanied by increased fluorescence signal of the proliferating cell marker Ki67 in *Mocos*$^{-/-}$ kidneys (Figure 6E, F). No sign of inflammation or fibrosis was detected in kidneys of heterozygous *Mocos* and wild type littermates at 4 weeks of age.

Impaired ability of xanthinuric animals to mount the biological response to overcome oxidative stress and inflammation

Because PPAR*γ* plays additional roles by participating in inflammation and oxidative stress in renal disease, we next examined redox homeostasis in *Mocos*$^{-/-}$ mice. Confirming further the potential antioxidative protective effect of PPARγ[29] (Figure 6A), we found that NOX4, a NADPH oxidase isoform expressed in proximal tubular cells and known to be an important source of ROS[30], was significantly underexpressed in *Mocos*$^{-/-}$kidney when compared to littermate controls (Figure7A). These possible renoprotective effects of NOX4 and PPARγ were accompanied by increased expression of glutamate-cysteine ligase (GCLC, the key enzyme in glutathione synthesis), but impaired activation of genes encoding many antioxidant and detoxifying enzymes known to be targets of PPAR γ and nuclear factor-erythroid-2-related factor 2 (Nrf2) (Figure 7B-F). Particularly noteworthy was the dysregulation of the thioredoxin (TXN)-based antioxidant system with the significant increase of thioredoxin-inhibitory protein (TXNIP) and thioredoxin-domain containing 12 (TXNDC12) which suggested a disruption of

the TXNIP-TXN complex and endoplasmic reticulum (ER) stress in *Mocos*$^{-/-}$ kidneys (Figure 7G-I and reference [31]). Finally, our data highlighted the importance of reactive carbonyl species (RCS) stress in affected *Mocos*$^{-/-}$ kidneys expressing aberrant levels of AKR1B8 and AKR1C1, two members of the aldo-keto reductase (AKR) superfamily involved in detoxification of cytotoxic carbonyls and balance of electrolytes and potassium respectively (Figure 7J-K).

Major dysfunctions of purine, aminoacids and phospholipids pathways in kidneys from xanthinuric *Mocos* mice

A metabolomics approach was next performed by liquid chromatography tandem high-resolution mass spectrometry method (LC-HRMS) to uncover altered metabolites and biological pathways in *Mocos*$^{-/-}$ kidneys. As illustrated in Figure 8 and Supplementary Table S1, no significant modification of metabolites was observed in kidney tissues from *Mocos*$^{+/-}$ mice compared with wild type mice. Conversely, *Mocos*$^{-/-}$ kidneys revealed significant metabolic perturbations: of the 121 robust metabolites analyzed, 40 metabolites were altered when compared with wild type mice and 31 metabolites showed perturbation of renal expression when the three *Mocos*$^{+/+}$, *Mocos*$^{+/-}$ and *Mocos*$^{-/-}$ kidney groups were compared (Figure 8 and Supplemental Figure 6). As expected, lack of *MOCOS* activity resulted in very low levels of uric acid and allantoin, the primary product of urate oxidation (Figure 8). In this pathway, xanthine and its distant precursors, such as inosine and adenine, were also affected. This result thus reinforced the finding that the main metabolic function of *Mocos* is restrained to the purine catabolism pathway. In parallel, in agreement with the role of *Mocos* in a physiological alternative to the "classic" pathway of NO formation from L-arginine, the integrity of the arginine-NO/urea system was also disturbed in *Mocos*$^{-/-}$ kidneys with a strong perturbation of citrulline and guanidoacetic acid (a precursor of creatine), two known

metabolites of the urea cycle (Table 1). Interestingly, Table 1 also highlights significantly altered metabolites involved in energy metabolism and mitochondrial function, such as trimethylammoniobutanoic acid, while the decreased cysteine metabolism might further denote oxidative damage in *Mocos* KO kidneys. Finally, other notably disturbed metabolic pathways include the phospholipid biosynthetic pathway indicative of massive membrane remodeling of renal cells and the serotonin pathway (5-hydroxyindole acetate) of tryptophan metabolism (Figure 8, Table 1 and Supplemental Table 2).

In summary, the metabolic analysis of *Mocos*$^{-/-}$ kidneys underscored the essential role of purines and highlighted the potential pathophysiological implications of the deregulation of amino acids (3 pathways) and phospholipids metabolisms (2 pathways) in kidneys of *Mocos*-deficient mice (Supplemental Figure 7).

Discussion

Xanthinuria is an underrecognized disorder that, in less than half of the affected people, is characterized by xanthine stones. This rare genetic disorder may be accompanied by hydronephrosis and eventually other complications of urolithiasis such as pyelonephritis. In our *Mocos* deficient mouse model of xanthinuria, the leading pathology is obstructive nephropathy. To our knowledge, such a pathology has not been reported in either type I or type II xanthinuria in human. Nonetheless, the *Mocos* mouse may serve as a model to study the pathogenesis of obstructive nephropathy. Remarkably**,** the signs of obstructive nephropathy found in *Mocos* KO mice do not differ from those reported in humans affected by other forms of obstructive nephropathies of variable etiology such as nephrocalcinosis following hyperphosphaturia or hypercalciuria, calcium oxalate nephropathy, urate nephropathy, myeloma kidney, or obstruction following drug crystals[32]. Recently, an attempt to classify crystal nephropathies was

proposed according to the localization of crystal deposits in the renal vasculature (type 1), the nephron (type 2) or the draining urinary tract (type 3)[33]. Regarding this classification, analysis of the morphological data of *Mocos* deficient mice suggests a prevalence of type 2 and a minor contribution of type 3 nephropathy.

The mechanisms of xanthine crystal precipitation are not resolved but may involve neutrophils interstitial and tubular inflammation with inflammatory cytokines together with precipitation of Tamm Horsfall proteins. Different crystals cause injury in numerous disorders and induce inflammation via the NLRP3 inflammasome and cell death[34]. In this study, Mulay et al found that crystals of calcium oxalate, monosodium urate, calcium pyrophosphate dihydrate and cystine may trigger caspase-independent cell death via TNF-α/TNFR1, RIPK1, RIPK3 and MLKL and initiate tissue injury and organ failure. However, tissue damage and inflammation induced by xanthine crystals have not been reported so far. In view of the tubular cell necrosis and interstitial inflammation in *Mocos* KO mice, activation of the inflammasome or other danger signal pathways are likely activated, causing inflammation. These pathways, including DNA sensing pathways, need further investigation to understanding the molecular mechanisms behind the cellular processes that contribute to the onset and development of the disease. To explain how *Mocos* deletion may cause xanthinuria type II, we suggest a two-step process involving i) an obstructive nephropathy due to production, poor solubility and intratubular precipitation of xanthine and ii) cell stress and death mediated by altered detoxification circuitry, impairment of nutrient delivery and waste product removal from kidney cells. The cellular stress elicited by these events causes inflammation triggering crystal formation, which may then enhance renal pathology**.**

In the *Mocos* deficient mouse model of obstructive nephropathy, renal stones and decreased renal function are associated with hypouricemia and altered detoxification circuitry. While xanthine stones may be proinflammatory and worsen renal function, several studies have

reported positive correlations between hyperuricemia, kidney inflammation and renal failure induced by urate crystal formation[35, 36]. However, hypouricemia caused by increased excretion or diminished reabsorption of filtered uric acid is also observed in human[37] and it is established that uric acid is the most abundant soluble antioxidant preserving endothelial function in situations of oxidative stress[38]. Inflammation and oxidative stress are known to be involved in the pathogenesis of chronic kidney disease in humans and in chronic renal failure in animal models. As far as kidney stone disease is concerned, particularly calcium oxalate, injury induced by high concentrations of oxalate in renal tubular epithelial cells is related to oxidative stress, tissue inflammation and mitochondrial dysfunction[39]. Our data show disruption of intrarenal redox homeostasis and are consistent with the essential role of MOCOS in aldehyde detoxification[19, 20] and the relevance of RCS metabolism in ROS-related renal injury[40, 41]. They point to the poor ability of xanthinuric animals to mount a protective response to overcome oxidative stress via inflammation

Metabolomics studies allowed the differential diagnosis of type I and type II classical xanthinuria. These studies have highlighted the role of the purine degradation pathway but also pathways involved in amino acid metabolism (such as tryptophan), vitamin B6, nicotinamide and possibly polyamine catabolism in patients with xanthinuria type II. Severe symptoms are rarely observed in patients with classical xanthinuria presenting usually mild signs. Despite conservation of purine metabolism, the significant differences between mice and man likely reflect divergent features of key stages of kidney development. Moreover, the level of uric acid in mice is lower than that in human because uricase, an enzyme present in mouse but not in human, degrades uric acid into allantoin. Thus, decreased XDH and uric acid levels in the immediate post-natal period in *Mocos* deficient mice may significantly affect renal development and amplify xanthinuria. Although neonatal Mocos KO mice cannot overcome

MOCOS deficiency, we assume that the 50% reduction of MOCOS expression in heterozygous mice might be sufficient for a normal renal and metabolic function in young and aged mice.

Beside its role in nephropathology, MOCOS is involved in complex disorders such as ASD[20-22]. Although metabolomic studies on complex disorders are far from definitive and unambiguous, analysis of the metabolome has shown great potential to uncover biomarkers for complex diseases such as ASD. Indeed, recent studies on urine from ASD patients have reported that several metabolic profiles associated with amino acids, purine metabolism, creatine metabolism, energy metabolism and oxidative stress could be involved in ASD[42,43].

In conclusion, the *Mocos* mouse model may enable an integrated understanding of of xanthinuric obstructive nephropathy and of common mechanisms underlying complex diseases such as metabolic disorders and ASD**.**

Disclosure

All authors have nothing to disclose.

Funding

This work was supported by CNRS, INSERM, University of Orleans, University of Tours and the European funding in Region Centre-Val de Loire (FEDER N°2016-00110366=BIO-TARGET 2015-2018 and FEDER N° EX005756 =BIO-TARGETII).

Acknowledgments

We would like to thank PHENOMIN and the Mouse Clinical Institute (ICS, Strasbourg, France) for the generation of *Mocos* KO mice. Our special thanks are going to François Erard and to Melody Thilloux and Mathilde Favrat for technical assistance and animal handling. We are also grateful to the Center for Typing and Archiving of Animal Models (TAAM, Orleans, France) and more specifically to Emilie Bouvier and Severine Grieszmann for taking care of the animals. We also thank the department “Analyse des Systemes Biologiques” (PST ASB, Universite de Tours, France) for their help with sample analyses.

Author contributions

Delphine Sedda: Conceptualization; Investigation. Claire Mackowiak: Conceptualization; Data curation; Formal analysis; Investigation. Julie Pailloux: Conceptualization; Investigation. Elodie Culerier: Conceptualization. Ana Dudas: Investigation. Pauline Rontani: Conceptualization; Investigation. Nicolas Erard: Investigation. Antoine Lefevre: Conceptualization. Sylvie Mavel: Conceptualization; Data curation; Formal analysis. Patrick Emond: Data curation; Formal analysis. Frederic Foucher: Conceptualization; Data curation. Marc Le Bert: Conceptualization. Valerie Quesniaux: Project administration. Michael Mihatsch: Conceptualization; Data curation; Formal analysis; Investigation; Writing - original draft; Writing - review and editing. Bernhard Ryfferl: Funding acquisition. Madeleine Erard-Garcia: Conceptualization; Data curation; Investigation; Project administration; Supervision; Validation; Writing - original draft; Writing - review and editing.

Supplemental material Table of Contents:

References

1. Bradbury MG, Henderson M, Brocklebank JT, Simmonds HA. Acute renal failure due to xanthine stones. *Pediatr Nephrol*. 1995;9:476-477
2. Chalmers RA, Watts RW, Pallis C, Bitensky L, Chayen J. Crystalline deposits in striped muscle in xanthinuria. *Nature*. 1969;221:170-171
3. Pacher P, Nivorozhkin A, Szabo C. Therapeutic effects of xanthine oxidase inhibitors: Renaissance half a century after the discovery of allopurinol. *Pharmacol Rev*. 2006;58:87-114
4. Ichida K, Matsumura T, Sakuma R, Hosoya T, Nishino T. Mutation of human molybdenum cofactor sulfurase gene is responsible for classical xanthinuria type ii. *Biochem Biophys Res Commun*. 2001;282:1194-1200
5. Yamamoto T, Moriwaki Y, Takahashi S, Tsutsumi Z, Tuneyoshi K, Matsui K, et al. Identification of a new point mutation in the human molybdenum cofactor sulferase gene that is responsible for xanthinuria type ii. *Metabolism*. 2003;52:1501-1504
6. Peretz H, Naamati MS, Levartovsky D, Lagziel A, Shani E, Horn I, et al. Identification and characterization of the first mutation (arg776cys) in the c-terminal domain of the human molybdenum cofactor sulfurase (hmcs) associated with type ii classical xanthinuria. *Mol Genet Metab*. 2007;91:23-29
7. Watanabe T, Ihara N, Itoh T, Fujita T, Sugimoto Y. Deletion mutation in drosophila ma-l homologous, putative molybdopterin cofactor sulfurase gene is associated with bovine xanthinuria type ii. *J Biol Chem*. 2000;275:21789-21792
8. Zhou Y, Zhang X, Ding R, Li Z, Hong Q, Wang Y, et al. Using next-generation sequencing to identify a mutation in human mcsu that is responsible for type ii xanthinuria. *Cell Physiol Biochem*. 2015;35:2412-2421
9. Murgiano L, Jagannathan V, Piffer C, Diez-Prieto I, Bolcato M, Gentile A, et al. A frameshift mutation in mocos is associated with familial renal syndrome (xanthinuria) in tyrolean grey cattle. *BMC Vet Res*. 2016;12:276
10. Mayr SJ, Mendel RR, Schwarz G. Molybdenum cofactor biology, evolution and deficiency. *Biochim Biophys Acta Mol Cell Res*. 2021;1868:118883
11. Anantharaman V, Aravind L. Mosc domains: Ancient, predicted sulfur-carrier domains, present in diverse metal-sulfur cluster biosynthesis proteins including molybdenum cofactor sulfurases. *FEMS Microbiol Lett*. 2002;207:55-61
12. Hille R, Hall J, Basu P. The mononuclear molybdenum enzymes. *Chem Rev*. 2014;114:3963-4038
13. Bittner F. Molybdenum metabolism in plants and crosstalk to iron. *Front Plant Sci*. 2014;5:28
14. Battelli MG, Bortolotti M, Polito L, Bolognesi A. The role of xanthine oxidoreductase and uric acid in metabolic syndrome. *Biochim Biophys Acta Mol Basis Dis*. 2018;1864:2557-2565
15. Ichida K, Amaya Y, Okamoto K, Nishino T. Mutations associated with functional disorder of xanthine oxidoreductase and hereditary xanthinuria in humans. *Int J Mol Sci*. 2012;13:15475-15495
16. Ives A, Nomura J, Martinon F, Roger T, LeRoy D, Miner JN, et al. Xanthine oxidoreductase regulates macrophage il1beta secretion upon nlrp3 inflammasome activation. *Nat Commun*. 2015;6:6555
17. Terao M, Romao MJ, Leimkuhler S, Bolis M, Fratelli M, Coelho C, et al. Structure and function of mammalian aldehyde oxidases. *Arch Toxicol*. 2016;90:753-780

18. Kundu TK, Velayutham M, Zweier JL. Aldehyde oxidase functions as a superoxide generating nadh oxidase: An important redox regulated pathway of cellular oxygen radical formation. *Biochemistry*. 2012;51:2930-2939
19. Terao M, Garattini E, Romao MJ, Leimkuhler S. Evolution, expression, and substrate specificities of aldehyde oxidase enzymes in eukaryotes. *J Biol Chem*. 2020;295:5377-5389
20. Feron F, Gepner B, Lacassagne E, Stephan D, Mesnage B, Blanchard MP, et al. Olfactory stem cells reveal mocos as a new player in autism spectrum disorders. *Mol Psychiatry*. 2016;21:1215-1224
21. Taheri M, Noroozi R, Aghaei K, Omrani MD, Ghafouri-Fard S. The rs594445 in mocos gene is associated with risk of autism spectrum disorder. *Metab Brain Dis*. 2020;35:497-501
22. Rontani P, Perche O, Greetham L, Jullien N, Gepner B, Feron F, et al. Impaired expression of the COSMOC/MOCOS gene unit in asd patient stem cells. *Mol Psychiatry*. 2020
23. Dieme B, Lefevre A, Nadal-Desbarats L, Galineau L, Madji Hounoum B, Montigny F, et al. Workflow methodology for rat brain metabolome exploration using nmr, LC-MS and GC-MS analytical platforms. *J Pharm Biomed Anal*. 2017;142:270-278
24. Lefevre A, Mavel S, Nadal-Desbarats L, Galineau L, Attucci S, Dufour D, et al. Validation of a global quantitative analysis methodology of tryptophan metabolites in mice using LC-MS. *Talanta*. 2019;195:593-598
25. Xia J, Wishart DS. Using metaboanalyst 3.0 for comprehensive metabolomics data analysis. *Curr Protoc Bioinformatics*. 2016;55:14 10 11-14 10 91
26. Babitt JL, Lin HY. Mechanisms of anemia in CKD. *J Am Soc Nephrol*. 2012;23:1631-1634
27. Meng XM, Nikolic-Paterson DJ, Lan HY. Tgf-beta: The master regulator of fibrosis. *Nat Rev Nephrol*. 2016;12:325-338
28. Humphreys BD. Mechanisms of renal fibrosis. *Annu Rev Physiol*. 2018;80:309-326
29. Ma Y, Shi M, Wang Y, Liu J. Ppargamma and its agonists in chronic kidney disease. *Int J Nephrol*. 2020;2020:2917474
30. Gorin Y. The kidney: An organ in the front line of oxidative stress-associated pathologies. *Antioxid Redox Signal*. 2016;25:639-641
31. Wu M, Li R, Hou Y, Song S, Han W, Chen N, et al. Thioredoxin-interacting protein deficiency ameliorates kidney inflammation and fibrosis in mice with unilateral ureteral obstruction. *Lab Invest*. 2018;98:1211-1224
32. Khan SR, Pearle MS, Robertson WG, Gambaro G, Canales,BK, Doizi S, et al. Kidney stones. *Nat Rev Dis Primers* 2016; 2: 16008
33. Mulay SR, Anders HJ. Crystal nephropathies: mechanisms of crystal-induced kidney injury. *Nat Rev Nephrol*. 2017; 4:226-240
34. Mualy SC, Kulkarni OP, Rupanagudi KV, Migliorini A, Darisipudi MN, Vilaysane A et al. Calcium oxalate crystals induce renal inflammation by NLRP3-mediated IL-1β secretion. *J Clin Invest* 2013;):236-246
35. Kang DH, Nakagawa T, Feng L, Watanabe S, Han L, Mazzali M, et al. A role for uric acid in the progression of renal disease. *J Am Soc Nephrol*. 2002;13:2888-2897
36. Mihai S, Codrici E, Popescu ID, Enciu AM, Albulescu L, Necula LG, et al. Inflammation-related mechanisms in chronic kidney disease prediction, progression, and outcome. *J Immunol Res*. 2018;2018:2180373
37. Nishizaki N, Fujinaga S, Hirano D, Kanai H, Kaya H, Ohtomo Y, et al. Hereditary renal hypouricemia: A cause of calcium oxalate urolithiasis in a young female. *Clin Nephrol*. 2012;77:161-16332.

38. Waring WS, McKnight JA, Webb DJ, Maxwell SR. Uric acid restores endothelial function in patients with type 1 diabetes and regular smokers. *Diabetes*. 2006;55:3127-3132
39. Tsuji H, Wang W, Sunil J, Shimizu N, Yoshimura K, Uemura H, Peck AB, Khan SR. Involvement of renin-angiotensin-aldosterone system in calcium oxalate crystal induced activation of NADPH oxidase and renal cell injury. World J Urol. 2016 Jan;34(1):89-95.
40. Miyata T, Kurokawa K, van Ypersele de Strihou C. Relevance of oxidative and carbonyl stress to long-term uremic complications. *Kidney Int Suppl*. 2000;76:S120-125
41. Ratliff BB, Abdulmahdi W, Pawar R, Wolin MS. Oxidant mechanisms in renal injury and disease. *Antioxid Redox Signal*. 2016;25:119-146
42. Gevi F, Zolla L, Gabriele S, Persico AM. Urinary metabolomics of young italian autistic children supports abnormal tryptophan and purine metabolism. *Mol Autism*. 2016;7:47
43. Liu A, Zhou W, Qu L, He F, Wang H, Wang Y, et al. Altered urinary amino acids in children with autism spectrum disorders. *Front Cell Neurosci*. 2019;13:7

Table 1: List of the top six main disturbed pathways, and the related dysregulated metabolites in kidneys from the 3 groups of mice (*Mocos*$^{+/+}$, *Mocos*$^{+/-}$ and *Mocos*$^{-/-}$ mice).

Pathway Name	Matched metabolites
Arginine and proline metabolism	Citrulline; Guanidoacetic acid; N-Acetyl-L-alanine; 4-Guanidinobutanoic acid
Purine metabolism	Xanthine; Inosine; Uric acid; Adenine
Lysine degradation	4-Trimethylammoniobutanoic acid; Pipecolic acid
Cysteine and methionine metabolism	5'-Methylthioadenosine; L-Cystine
Glycerophospholipid metabolism	Phosphorylcholine; O-Phosphoethanolamine
Glycine, serine and threonine metabolism	Glyceric acid; Guanidoacetic acid

FIGURE LEGENDS

Figure 1. knockout of *Mocos* induces a partial phenotype in mice. (**A**) Schematic representation of the *Mocos* disruption strategy using the CRISPR/Cas9 technology. The deletion of exon 3 induces the loss of frame in case of splicing between exon 2 and exon 4 resulting in a truncated non-functional MOCOS protein. (**B**) Relative *Mocos* expresssion was quantified by qPCR; Data were from mice at 4 weeks of age and expressed as means±SEM, ***P*<,0.01.(**C**) Renal expression and quantification of MOCOS protein by western blot (data were from 4 week-old animals). (**D**) Frequency distribution of animals of the indicated genotype. The percentages of male (M) and female (F) mice of each genotype are indicated. (**E**) Phenotypic comparison of wild type$^{+/+}$, heterozygous *Mocos*$^{+/-}$ and knockout *Mocos*$^{-/-}$ mice. *Mocos*$^{-/-}$ animals are easily distinguished from littermates at 4 weeks because of their lower body size and weight. (**F**) Body weight of mice at 4weeks of age. 12 to 17 animals per group were analyzed. Data were expressed as means±SEM, ****P*<0.001. (G) Percentage of survival of wild-type (circle, n=168), heterozygote (square, n=239), and *Mocos*$^{-/-}$ (triangle, n=15) mice in days after birth. (H) Lifespan of *Mocos*$^{-/-}$ mice (n=15).

Figure 2. *Mocos* knockout induces obstructive nephropathy. (**A**) Representative images of whole kidney sections of mice at the age of 4 weeks. KO kidney shows an irregular outer contour due to numerous scars (indentions (arrows) and cystoid tubules (right, H&E stain). Control kidney (left, trichrome stain). By planimetry the size oft he KO kidneys was reduced by 50% on average. (**B**) KO Mouse: prominent interstitial fibrosis (blue staining cortex, trichrome stain and numerous cystoid tubules, mainly cortical collecting ducts (left), subcapsular scar with densly packed glomeruli (encircled), interstitial fibrosis, scanty

interstitial infiltrates. (right, HE stain). (**C**) Tubulo-interstitial space with dilated tubules, some with polymorphonuclear leukocytes (arrow) or lamellate bodies (uromodulin) (arrowheads), intratubular giant cell (x) and loss of tubular epithelium, (left ,HE stain). Right top: lamellate roundish intratubular deposit (stained for uromodulin with immunohistochemistry, brown) note adjacent tubule stuffed full with polymorphonuclear leukocytes. Right bottom: Empty crystal clefts in tubules (arrow), (semithin section stained with methylene blue). (**D**) Kidney cross-section similar to Fig A an B. Papillary tip and on the opposite side renal pelvis covered by uromodulin (x). The ducts in the papillary tip are highly dilated and contain lamellate bodies. (left, HE stain).Right higher magnification of the pelvic wall: Note damage of the urothelium with denudation(between arrows) oft the pelvic smooth muscle wall (arrow). The adjacent urothelium is preserved (U). (magnification in all figures: bar= µm)

Figure 3. Constitutive *MOCOS* KO mice accumulate xanthine stones. (**A**) The picture shows representative images of the transparent urine of homozygous *Mocos*$^{-/-}$ mice compared to the yellow color of urine characterizing wild type and heterozygous *Mocos*$^{+/-}$ mice. The arrow points to deposits in urine from a *Mocos*$^{-/-}$ mouse. (**B**) Measurement of urinary pH in mouse strains. Data were from mice at 4 weeks of age and expressed as means±SEM, $^{**}P<0.01$. (**C**) Concentrations of xanthine and hypoxanthine are significantly increased in urine and (**D**) serum of homozygous *Mocos*$^{-/-}$ mice compared with age-matched littermate controls. Data were from mice at 4 weeks of age and expressed as means±SEM, $^{*}P<0.05$, $^{**}P<0.01$. (**E**) The picture is an example of xanthine stones from a *Mocos*$^{-/-}$ mouse. Scale bars: 200 µm. (**F**) Crystals collected from a *Mocos*$^{-/-}$ kidney were analyzed by Raman spectroscopy. In these crystals, the strongest bands observed at 542, 653, 960, 1208, 1264, 1330 and 1433cm^{-1} are considered as marker bands of xanthine (lower green panel) by comparison with a commercial standard (upper blue panel).

Figure 4. Inactivation of *Mocos* leads to impaired renal and hepatic functions. Analysis of serological parameters including (**A**) creatinine, (**B**) urea, (**C**) uric acid, (**D**) alanine aminotransferase (ALAT), (**E**) alkaline phosphatase and (**F**) aspartate aminotransferase (ASAT) from 4 week–old animals. *Mocos*$^{-/-}$ mice were compared with heterozygous *Mocos*$^{+/-}$ and wild type littermate controls (n= 5 for each genotype). Each bar represents the means ±SEM, **P*<0.05, ***P*<0.01.

Figure 5. *Mocos*$^{-/-}$ mice display anemia. White blood cells counts and differential counts performed to identify the type of leukocytes are given as a percentage. The haematogram of homozygous *Mocos*$^{-/-}$ mice was compared with that of littermate controls at 4-week of age. The reference range for each group of parameter is indicated. Data are means±SEM, ***P*<0.01, ****P*<0.001.

Figure 6. *Mocos* gene disruption induces expression of adipogenesis-related genes, inflammatory response and interstitial fibrosis in *Mocos*$^{-/-}$ kidney. (**A**) Enhanced expression of C/EBP-β and PPARγ in *Mocos* KO mice compared with controls. Transcription was measured by RT-PCR in 4 week-old mice. Data are expressed as means±SEM, **P*< 0.05. (**B**) Genes involved in inflammatory response were significantly upregulated in *Mocos* KO kidneys when compared with kidneys from littermate controls. Expression levels of TNFα and MCP1/CCL2 were measured by RT-PCR. Data were from mice at 4 weeks of age and expressed as means±SEM, **P*< 0.05, ***P*< 0.01. (**C)** Disruption of the *Mocos* gene induced renal interstitial fibrosis. The expression levels of TGFβ1 and serpine/PAI1 were measured by RT-PCR in 4-week–old mice (n=5 for each genotype). Results are expressed as means±SEM, * *P*< 0.05, ** *P*< 0.01. (**D**) TUNEL staining shows apoptosis of tubular epithelial cells in kidneys

from *Mocos*$^{-/-}$ mice (scale bar: 100μm). (**E**) Immunofluorescence staining of Ki67 revealed markedly increased cell proliferation in kidneys of *Mocos* KO mice at 4-weeks of age when compared to controls. DAPI was used to label nuclei. (**F**) Quantitation of cell proliferation was determined by counting the number of Ki67 positive nuclei in each mouse strain of the specified genotypes.

Figure 7. *Mocos* deletion alters detoxification defenses in kidney. (**A**) Disruption of *Mocos* induces decreased expression levels of NOX4 and (**B**) increased transcription of GCLC but no modification of genes encoding several antioxidant and detoxifying enzymes such as (**C**) NQO1, (**D**) GPX1, (**E**) SOD1 and (**F**) GLO1 in *Mocos*$^{-/-}$ kidneys when compared to littermate controls. (**G-H**) The transcription of TXN was not affected but the TXN complex was umbalance with significant upregulation of TXNIP in xanthinuric mice. (**I**) Expression of TXNDC12 dithiol-disulfide oxidoreductase of the endoplasmic reticulum and (**J**) AKR1B8, an aldoketoreductase involved in carbonyl detoxification was significantly upregulated in *Mocos*$^{-/-}$ mice but not in wild type and heterozygotes mice. All results were obtained by RT-PCR in kidneys of 4-week–old mice (n=4 to 7 for each genotype). Results were expressed as means±SEM, **P*< 0.05, ***P*< 0.01. (K*)* Renal expression of AKR1C1 is significantly disturbed in *Mocos* KO mice when compared to controls (western blot).

Figure 8. Metabolome analysis of kidneys from *Mocos*$^{-/-}$ mice and littermate controls. Heat map depicting the top 31 most significantly affected metabolites, where red indicates an increase concentration and blue indicates a decrease. Kidneys from young *Mocos*$^{-/-}$ mice (class C) were compared to kidneys from *Mocos*$^{+/-}$ (class B) and wild type littermates (class A) (distance measure using Euclidean, and clustering algorithm using Ward).

Figure 1

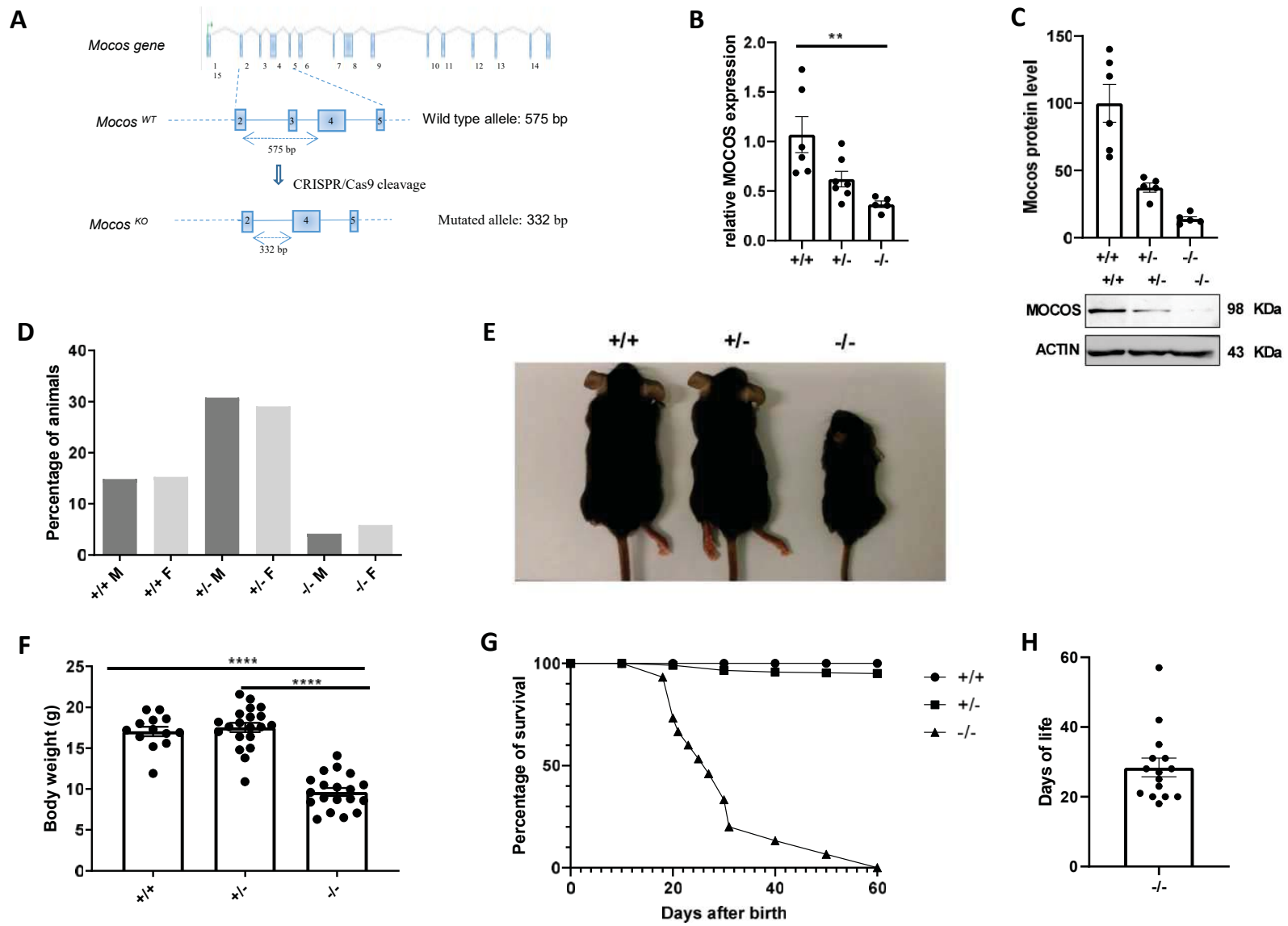
A
Mocos gene
Mocos WT
Wild type allele: 575 bp
575 bp
CRISPR/Cas9 cleavage
Mocos KO
Mutated allele: 332 bp
332 bp
B
relative MOCOS expression
**
+/+
+/-
-/-
C
Mocos protein level
MOCOS
ACTIN
98 KDa
43 KDa
D
Percentage of animals
+/+ M
+/+ F
+/- M
+/- F
-/- M
-/- F
E
+/+
+/-
-/-
F
Body weight (g)
****
****
G
Percentage of survival
Days after birth
H
Days of life

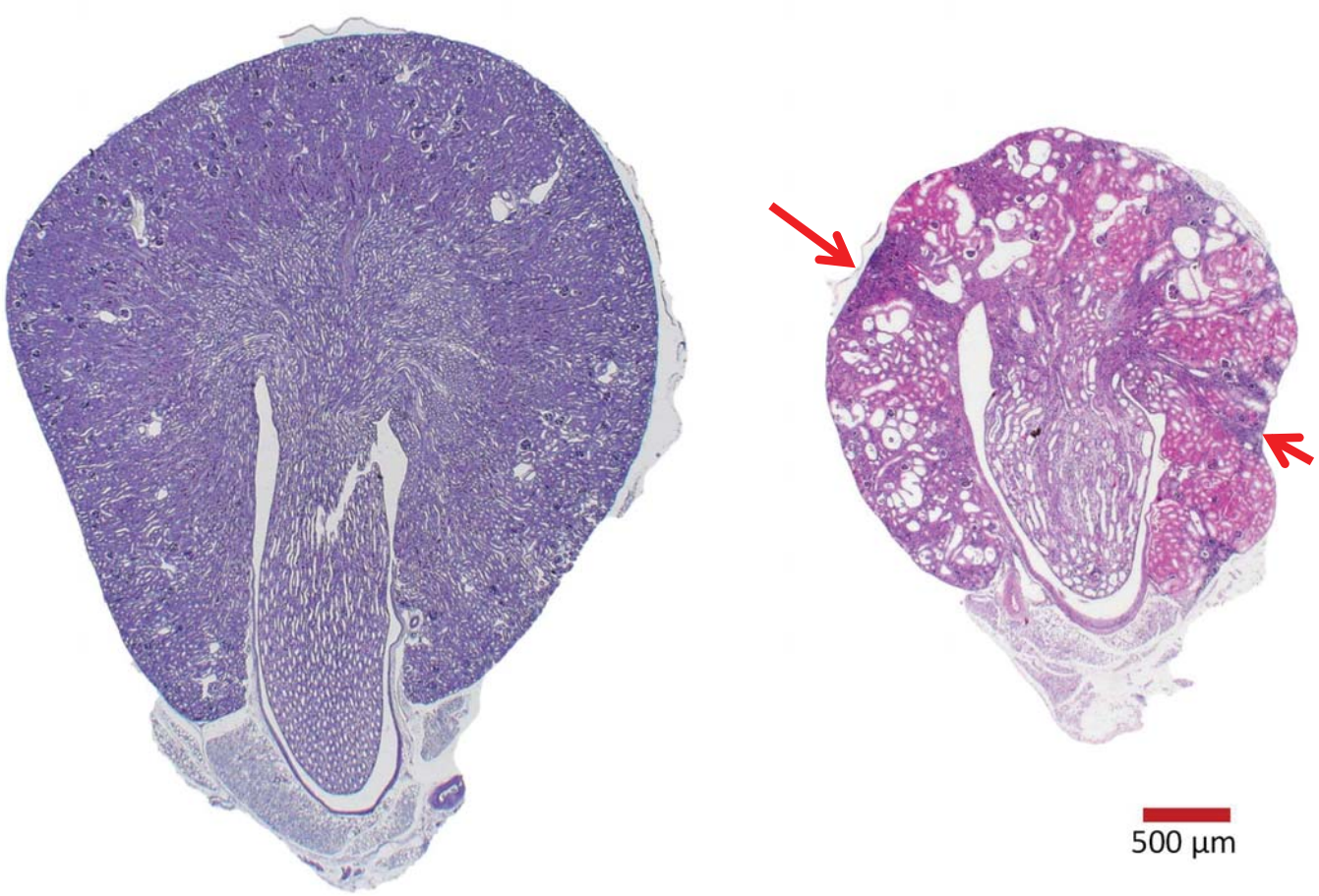

Figure 2A

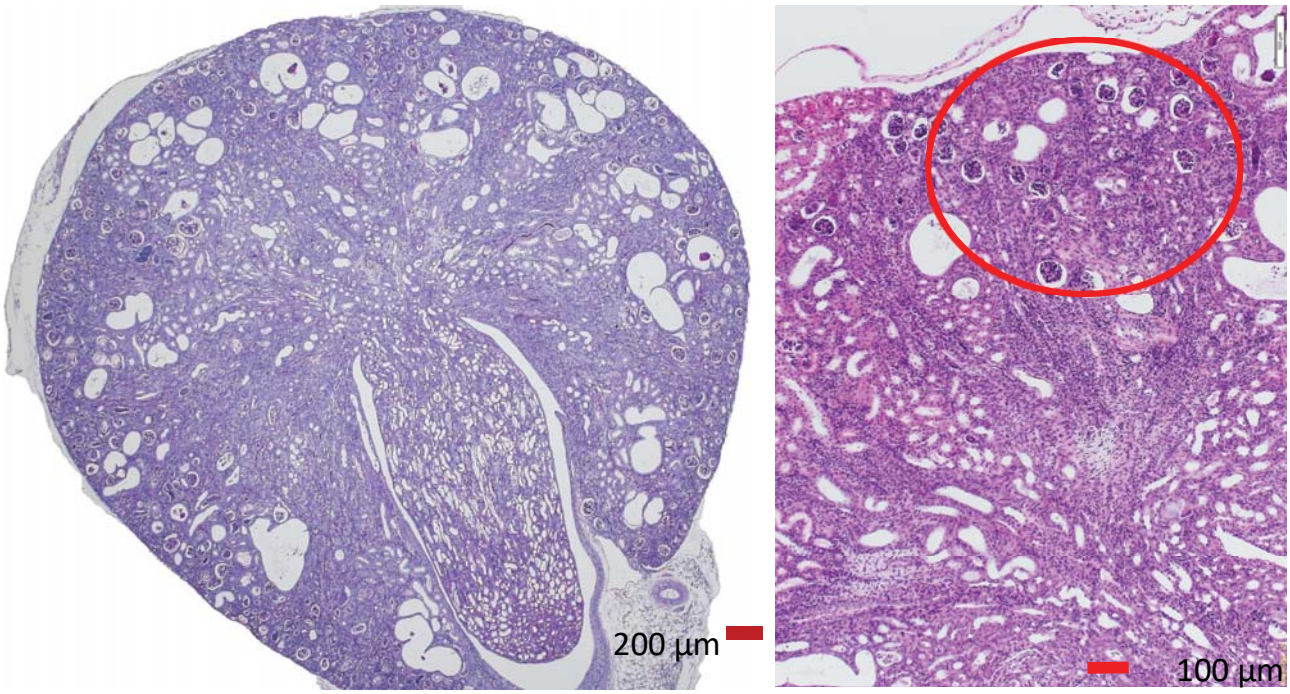

Figure 2B

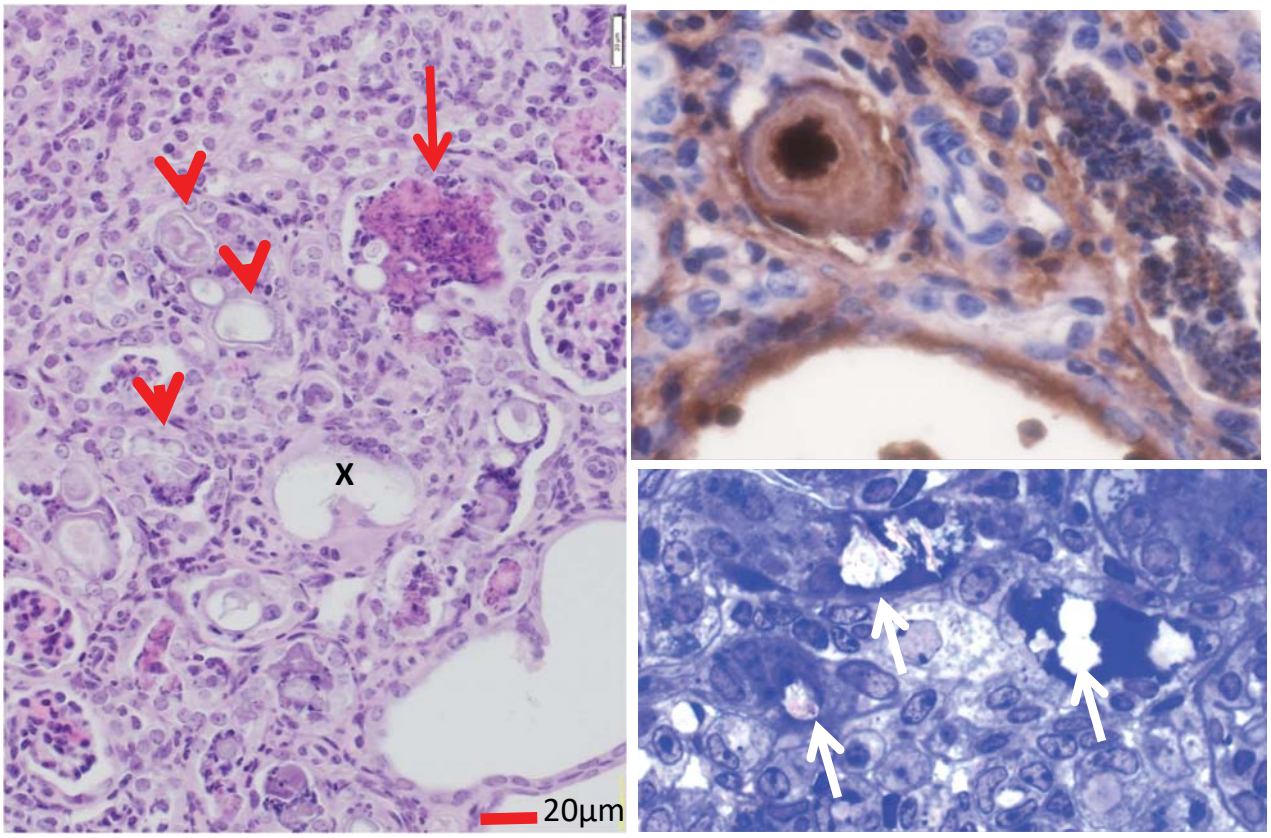

Figure 2C

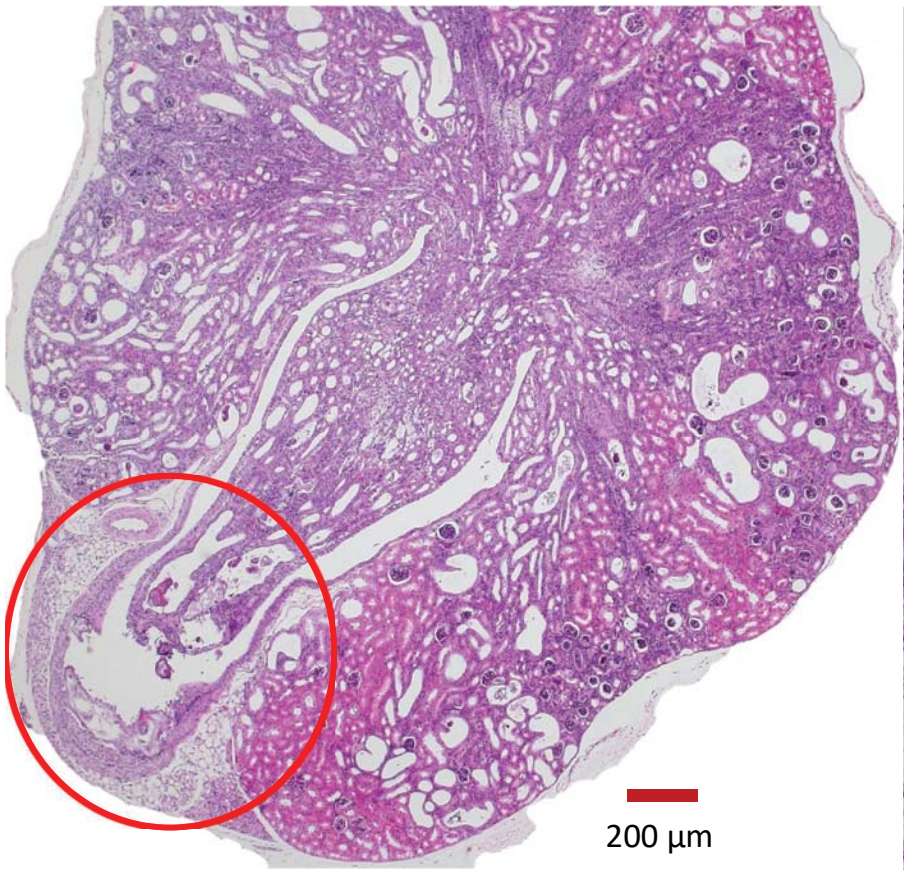

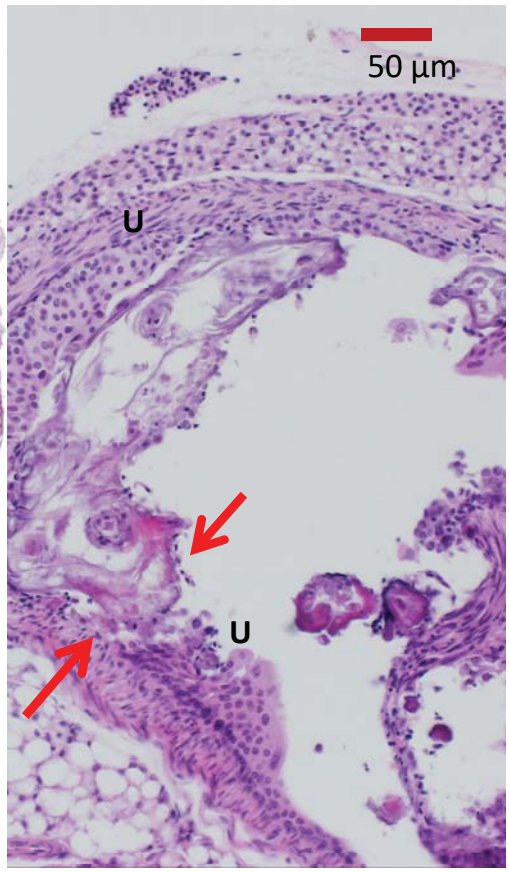

Figure 2D

Figure 3

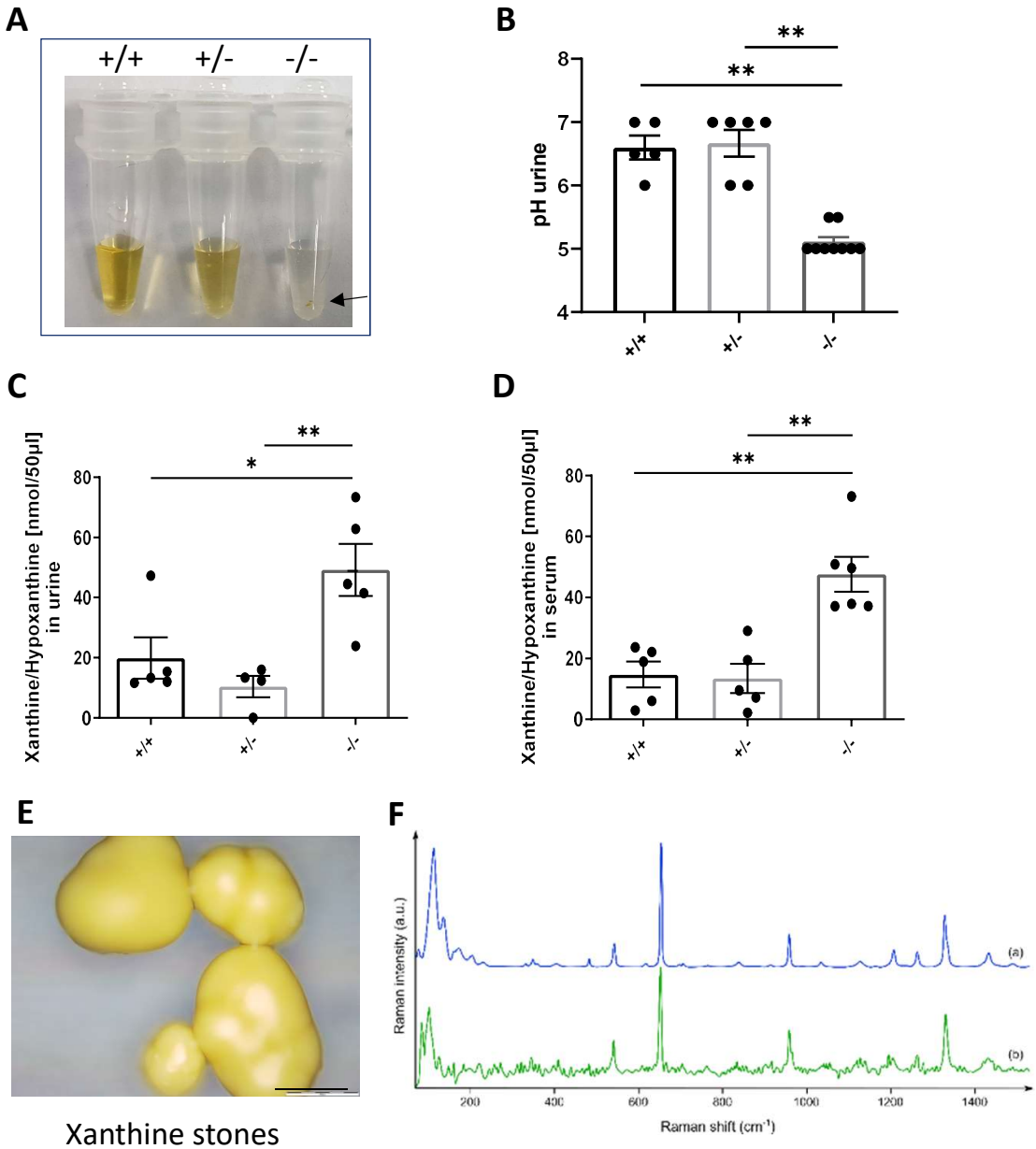

Xanthine stones

Figure 4

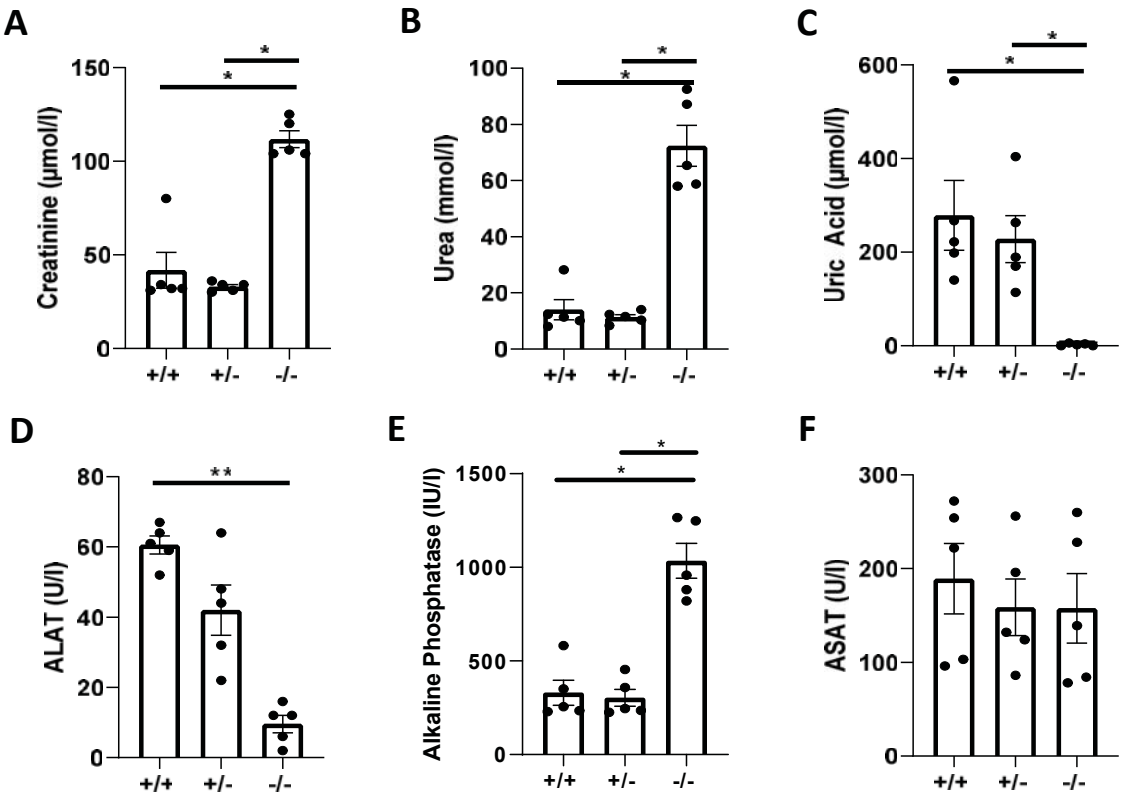
A
Creatinine (µmol/l)
150
100
50
0
+/+
+/-
-/-
*
*
B
Urea (mmol/l)
100
80
60
40
20
0
+/+
+/-
-/-
*
*
C
Uric Acid (µmol/l)
600
400
200
0
+/+
+/-
-/-
*
*
D
ALAT (U/l)
80
60
40
20
0
+/+
+/-
-/-
**
E
Alkaline Phosphatase (IU/l)
1500
1000
500
0
+/+
+/-
-/-
*
*
F
ASAT (U/l)
300
200
100
0
+/+
+/-
-/-

Figure 5

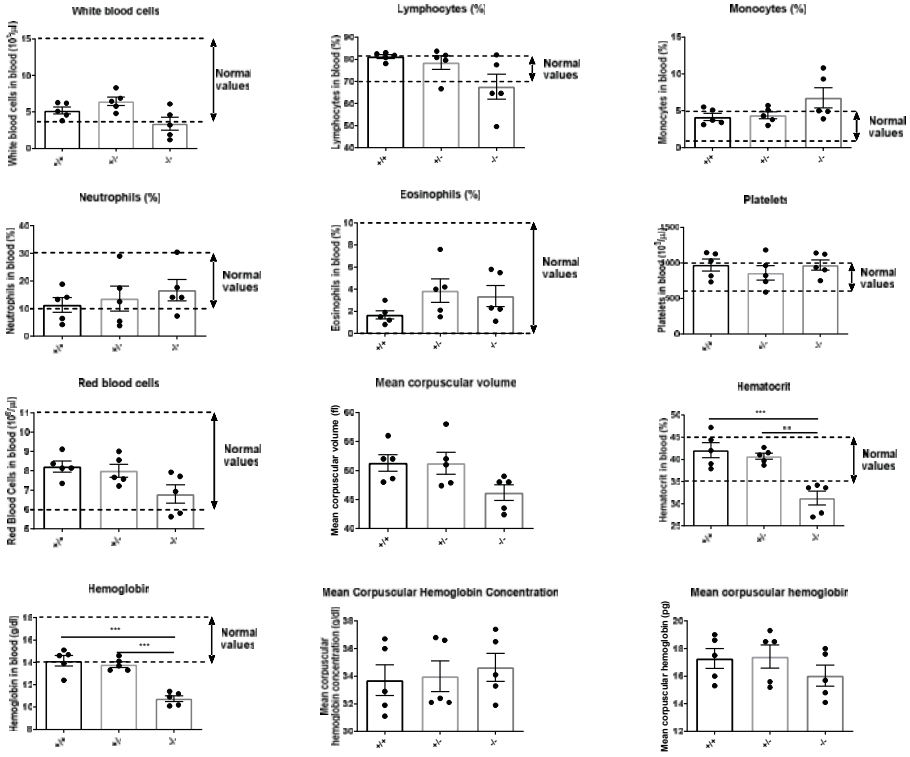
White blood cells
White blood cells in blood (10³/µl)
Normal values
Lymphocytes (%)
Lymphocytes in blood (%)
Normal values
Monocytes (%)
Monocytes in blood (%)
Normal values
Neutrophils (%)
Neutrophils in blood (%)
Normal values
Eosinophils (%)
Eosinophils in blood (%)
Normal values
Platelets
Platelets in blood (10³/µl)
Normal values
Red blood cells
Red Blood Cells in blood (10⁶/µl)
Normal values
Mean corpuscular volume
Mean corpuscular volume (fl)
Hematocrit
Hematocrit in blood (%)
Normal values
Hemoglobin
Hemoglobin in blood (g/dl)
Normal values
Mean Corpuscular Hemoglobin Concentration
Mean corpuscular hemoglobin concentration (g/dl)
Mean corpuscular hemoglobin
Mean corpuscular hemoglobin (pg)

Figure 6

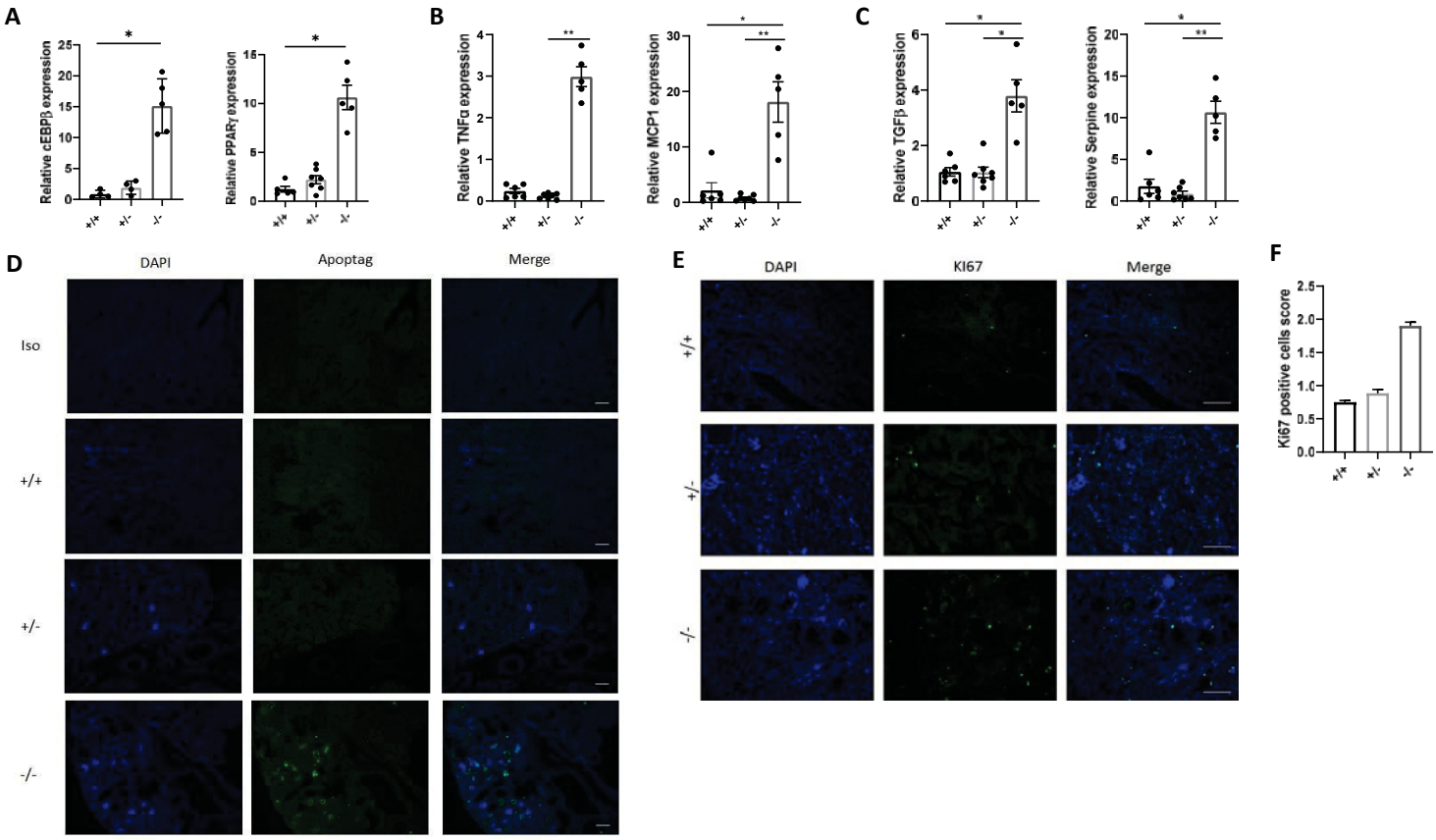
A
Relative cEBPβ expression
Relative PPARγ expression
B
Relative TNFα expression
Relative MCP1 expression
C
Relative TGFβ expression
Relative Serpine expression
+/+
+/-
-/-
D
DAPI
Apoptag
Merge
Iso
+/+
+/-
-/-
E
DAPI
KI67
Merge
+/+
+/-
-/-
F
Ki67 positive cells score

Figure 7

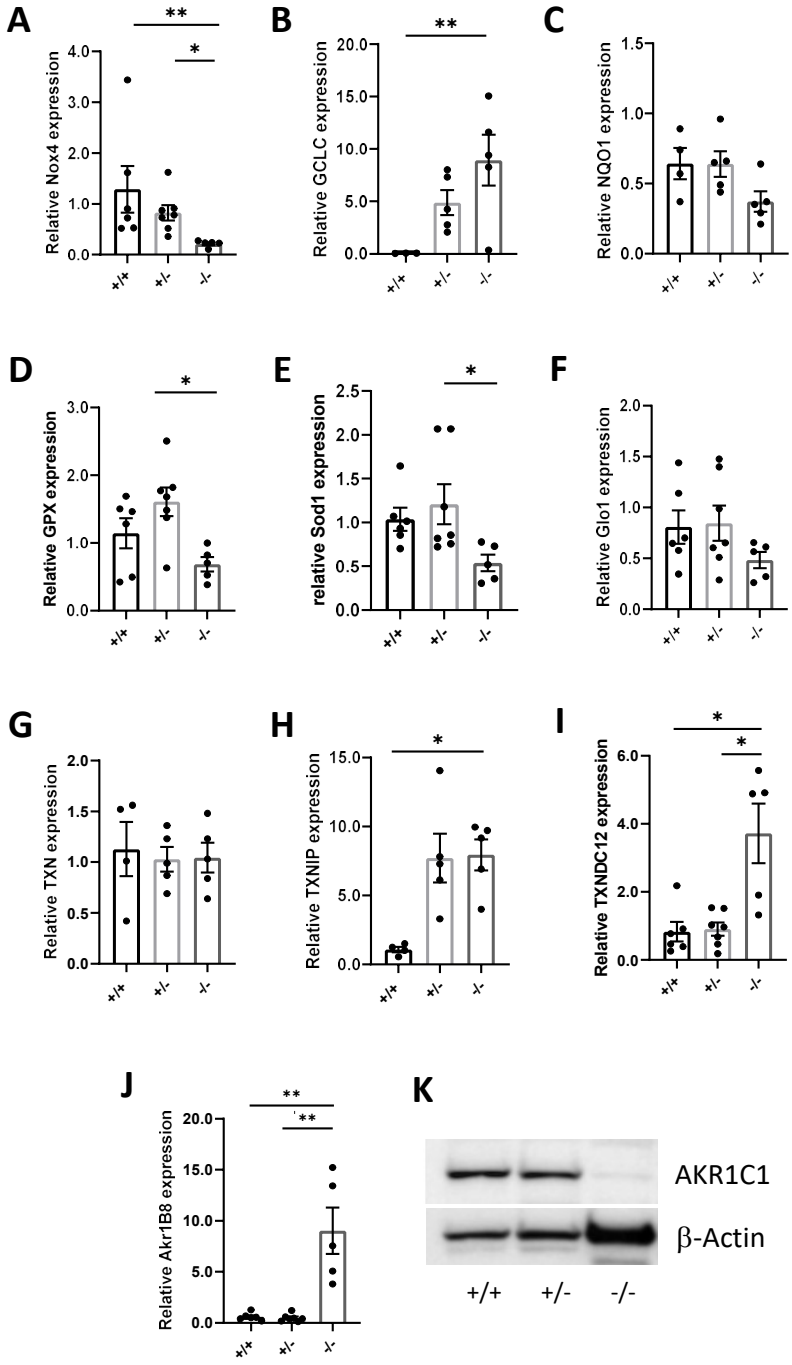
A
Relative Nox4 expression
B
Relative GCLC expression
C
Relative NQO1 expression
D
Relative GPX expression
E
relative Sod1 expression
F
Relative Glo1 expression
G
Relative TXN expression
H
Relative TXNIP expression
I
Relative TXNDC12 expression
J
Relative Akr1B8 expression
K
AKR1C1
β-Actin
+/+
+/-
-/-

Figure 8

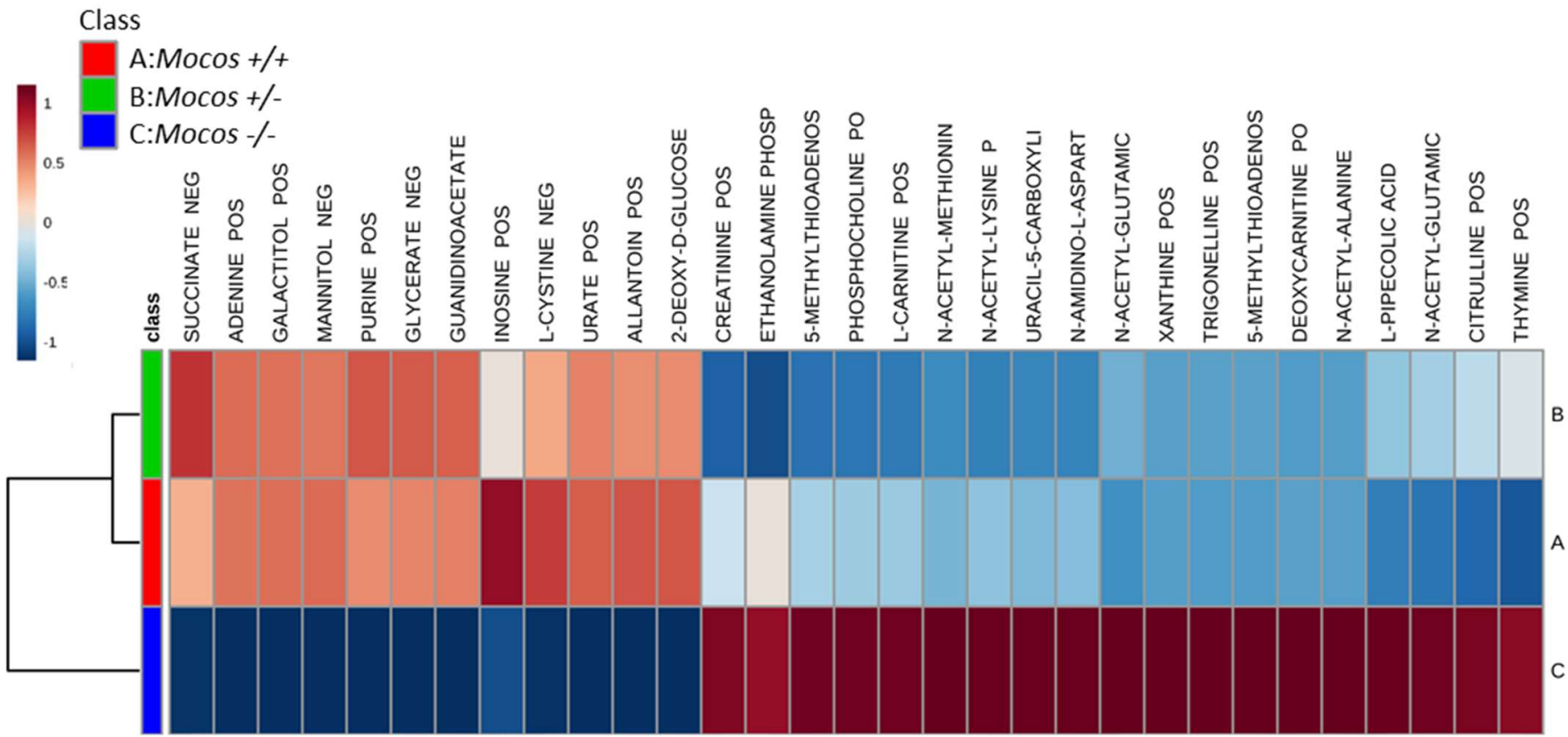
Class
A:Mocos +/+
B:Mocos +/-
C:Mocos -/-
1
0.5
0
-0.5
-1
class
SUCCINATE NEG
ADENINE POS
GALACTITOL POS
MANNITOL NEG
PURINE POS
GLYCERATE NEG
GUANIDINOACETATE
INOSINE POS
L-CYSTINE NEG
URATE POS
ALLANTOIN POS
2-DEOXY-D-GLUCOSE
CREATININE POS
ETHANOLAMINE PHOSP
5-METHYLTHIOADENOS
PHOSPHOCHOLINE PO
L-CARNITINE POS
N-ACETYL-METHIONIN
N-ACETYL-LYSINE P
URACIL-5-CARBOXYLI
N-AMIDINO-L-ASPART
N-ACETYL-GLUTAMIC
XANTHINE POS
TRIGONELLINE POS
5-METHYLTHIOADENOS
DEOXYCARNITINE PO
N-ACETYL-ALANINE
L-PIPECOLIC ACID
N-ACETYL-GLUTAMIC
CITRULLINE POS
THYMINE POS
B
A
C

Original Article

Supplemental Material

Deletion of *Mocos* induces xanthinuria with obstructive nephropathy and major metabolic disorders in mice

Delphine Sedda et al.

Supplemental Methods

Histological and Immunofluorescence Analysis

Dissected tissues were fixed in 4% buffered paraformaldehyde and paraffin embedded under standard conditions. Tissue sections (3 µm) were stained with hematoxylin and eosin. The slides were examined blindly by 2 independent investigators with a Nikon microscope (Nikon eclipse 80i; Nikon, Tokyo, Japan) or with stereomicroscope (Leica M80).

For Immunofluorescence, tissues were fixed for 3 days in 4% PFA and submerged in 20% sucrose for 1 week. They were then embedded in OCT (Tissue-Teck) and 10 µM sections were prepared with cryotome (Leica). TUNEL staining was performed on sections using the ApopTag® Fluorescein In Situ Apoptosis Detection kit (Merck, S7110) following manufacturer's protocol. For Ki67 (PCNA) staining, slides were incubated 30 min in citrate buffer at 80 °C, washed in TBS-Tween and then incubated overnight with rabbit-anti-mouse-Ki67 (Abcam, 4 µg/ml, ab15580). After washing with slides were treated with 0,05% pontamin sky blue (Sigma) for 15 min and then incubated with secondary goat anti-rabbit antibody (Abcam ,2µg/mL, ab150077) for 45 min at room temperature. After washing, slides were

incubated with DAPI (Fisher Scientific) and mounted in fluoromount® (SouthernBiotech). Tissue sections were analysed on a Leicafluorescence microscope Leica (Leica, CTR6000) at x200 magnification. The slides were analyzed and semi-quantitatively scored.

Metabolic analysis

Metabolic analysEs were performed by liquid chromatography coupled with high resolution mass spectrometry (LC-HRMS) based on standard metabolomics approaches. Briefly, frozen kidney tissue samples were lyophilized during 48 h and milled to a fine powder. Two milligrams of ground samples were extracted with 1.5 mL of Methanol/milliQ water (1/1). After centrifugation, the supernatants were collected and concentrated at 35°C for 2h30. the analyses were done on a UPLC Ultimate 3000 system (Dionex), coupled to a Q-Exactive mass spectrometer (Thermo Fisher Scientific, Germany) and operated in positive (ESI+) and negative (ESI−)electro spray ionization modes. Chromatography was carried out with a PhenomenexKinetex1.7mXB C18 (150mm×2.10mm) and 100Å UHPLC column. The solvent system comprised mobile phase A [0.1% (vol/vol) formic acid in water], and mobile phase. Data were processed using Xcalibur® software (Thermo Fisher Scientific, San Jose, CA). A library of standard compounds (Mass Spectroscopy Metabolite Library of Standards MSMLS supplied by IROA TechnologiesTM) were analyzed with the same conditions and gradient of mobile phases than those used to analyze the extracted metabolites. For data processing, briefly, peaks with greater than 30% variance (CV %) in quality control samples were removed. The normalization was done to the total area of the peaks of interest. The multivariate analyses were done using Simca-P+-15 software (Umetrics, Umeå, Sweden) as previously described[36]. Briefly, the data analyses were first conducted using principal component analysis (PCA) to detect outliers. Discriminant metabolites were obtained after orthogonal partial least squares discriminant analysis (OPLS-DA), after elimination of metabolites with low impact in the

separation of the different groups. The listing of discriminant metabolites [very important in projection (VIP)] is given in supplementary data, Table S1. Univariate analyses were performed as non-parametric tests (Wilcoxon rank-sum test) using the web free server Metaboanalyst (https://www.metaboanalyst.ca/) with an FDR adjusted p-value of 0.05 (see listing of significant metabolites in supplementary data, Table S1). VIP and significant metabolites were introduced in pathways analysis module in MetaboAnalyst. Pathways showing the lowest p-value, with an impact value different from zero were chosen from the pathway topology analysis.

Legends of Supplemental figures

Supplemental Figure 1.

Heterozygous Mocos mice develop normally but *Mocos* KO mice display major morphologic abnormalities in kidney, liver and brain. (**A**) Body weight evolution in adult heterozygous *Mocos* mice and wild type littermates of 8, 10 and 12 month of age. (**B**) Pictures showing the small size and irregular surface of a *Mocos*$^{-/-}$ kidney (by planimetry the size of *Mocos*$^{-/-}$ kidneys are reduced by 50 % on average when compared to controls). (**C**) *Mocos* KO mice (n=10) had significantly decreased kidney weights and kidney to body weight ratios, compared with their control littermates at 4 weeks of age (n=6). (**D-H**) Organ weight and organ//body weight ratio were all assessed in mice at 4 weeks of age. Data are expressed as means ± SEM, **P*<0.05, ***P*<0.01, ****P*<0.001.

Supplemental Figure 2.

Deletion of *Mocos* causes occasional hydronephrosis in homozygous mutants surviving until 2 months. H&E staining of kidney sections with highly atrophic parenchymal rim (left

panel, scale bar: 1mm). The area within the rectangle is shown under higher magnification in the right panel (scale bar: 100µm).

Supplemental Figure 3.

***Mocos* disruption does not change the histology of organs except the kidney in young mice**. H&E staining of (**A**) liver and (**B**) lung sections from 4 week-old *Mocos*$^{-/-}$ mice and littermate controls (scale bar: 100µm). (**C and D**) Staining of kidney sections from 8- and 10 month-old heterozygous *Mocos* mice compared with wild type littermates. (**E and F**) Staining of liver sections from 8 and 10 month-old heterozygous *Mocos* mice compared with wild type controls (scale bar: 100µm).

Supplemental Figure 4.

Adult heterozygous *Mocos* mice display no disturbances of renal function. Analysis of serological parameters including (**A**) creatinine, (**B**) urea, (**C**) uric acid, (**D**) alanine aminotransferase (ALAT), (**E)** alkaline phosphatase and (**F**) aspartate aminotransferase (ASAT). Sera from young and adult *Mocos*$^{+/-}$ mice were compared with those from littermate control mice. Each bar represents the mean ± SEM.

Supplemental Figure 5.

Adult heterozygous *Mocos* mice exhibit normal hematological parameters. Hematological parameters of *Mocos*$^{+/-}$ mice were compared with those of wild type mice at 15- and 20- months.

Supplemental Figure 6.

Clustering result shown as heatmap for the discriminant metabolites in kidney from the 3 groups of *Mocos* $^{+/+}$, *Mocos* $^{+/-}$ and *Mocos* $^{-/-}$ mice.

Supplemental Figure 7

The purine and arginine/nitric oxide pathways in xanthinuric mice. AMP (adenosine monophosphate); IMP (inosine monophosphate); GMP (guanosine monophosphate); NO (nitric oxide); PNP1 (purine nucleoside phosphorylase1); GDA (guanine desaminase); UOX1 (urate oxidase1); OTC (ornithine transcarbamylase); NOS (nitric oxide synthase); ARG1 (arginase1); XOR (Xanthine oxidoreductase); AOX1 (aldehyde oxidase1).

Supplemental Table 1.

List of primers

Supplemental Table 2.

Listing of discriminant metabolites obtained after univariate analysis [Wilcoxon rank-sum test with an FDR adjusted p-value of 0.05, visualized by *) cumulated with VIP discriminant metabolites obtained after OPLS-DA (visualized by √), CV-ANOVA of the model was given in the first row of the table] from kidney tissues analysis of wildtype, *Mocos*$^{+/-}$ and KO mice.

Supplemental Figure 1

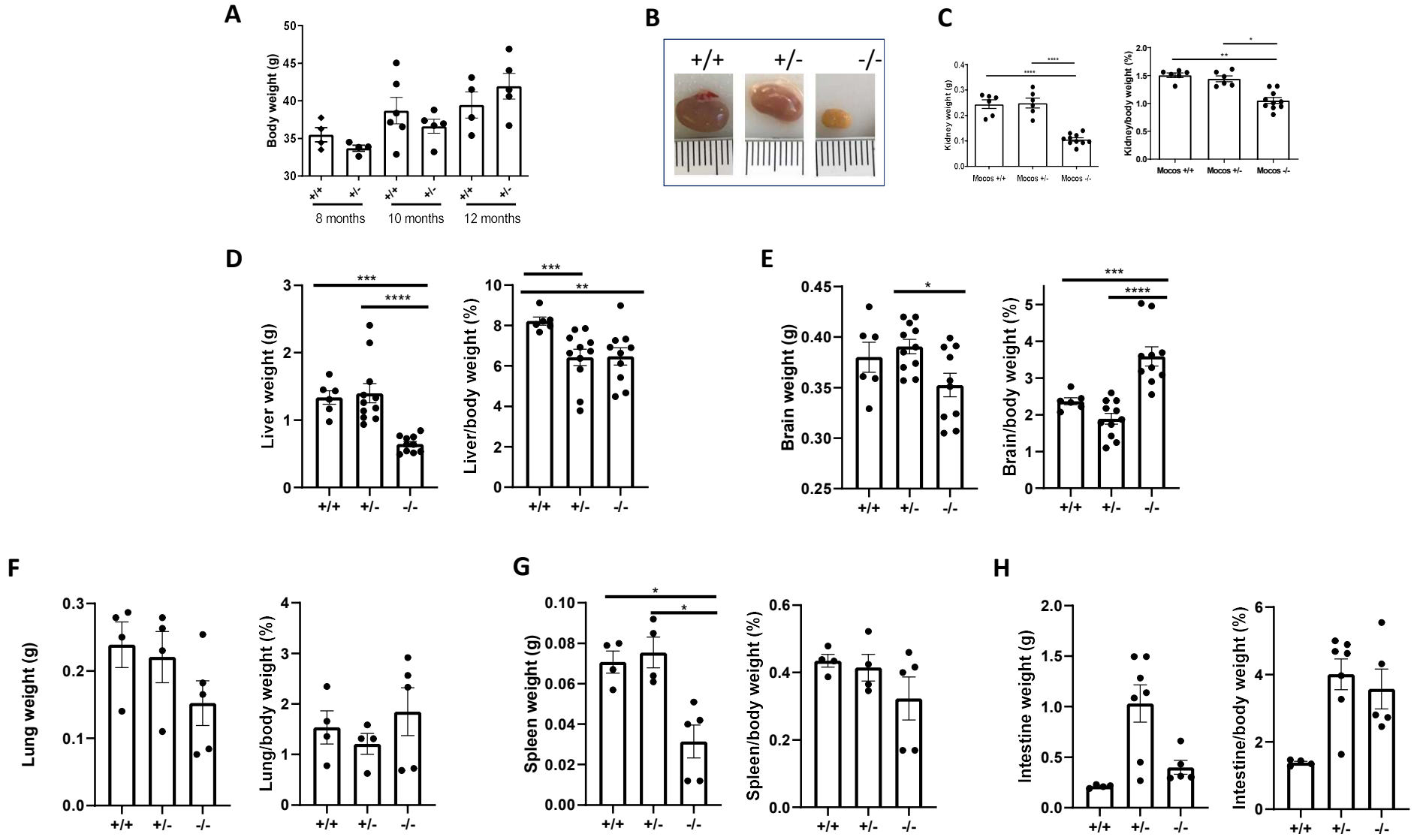

Supplemental Figure **2**

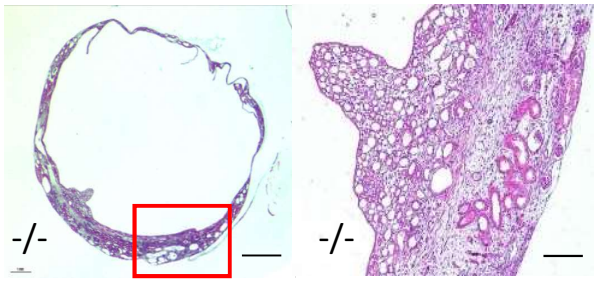

Supplemental Figure 3

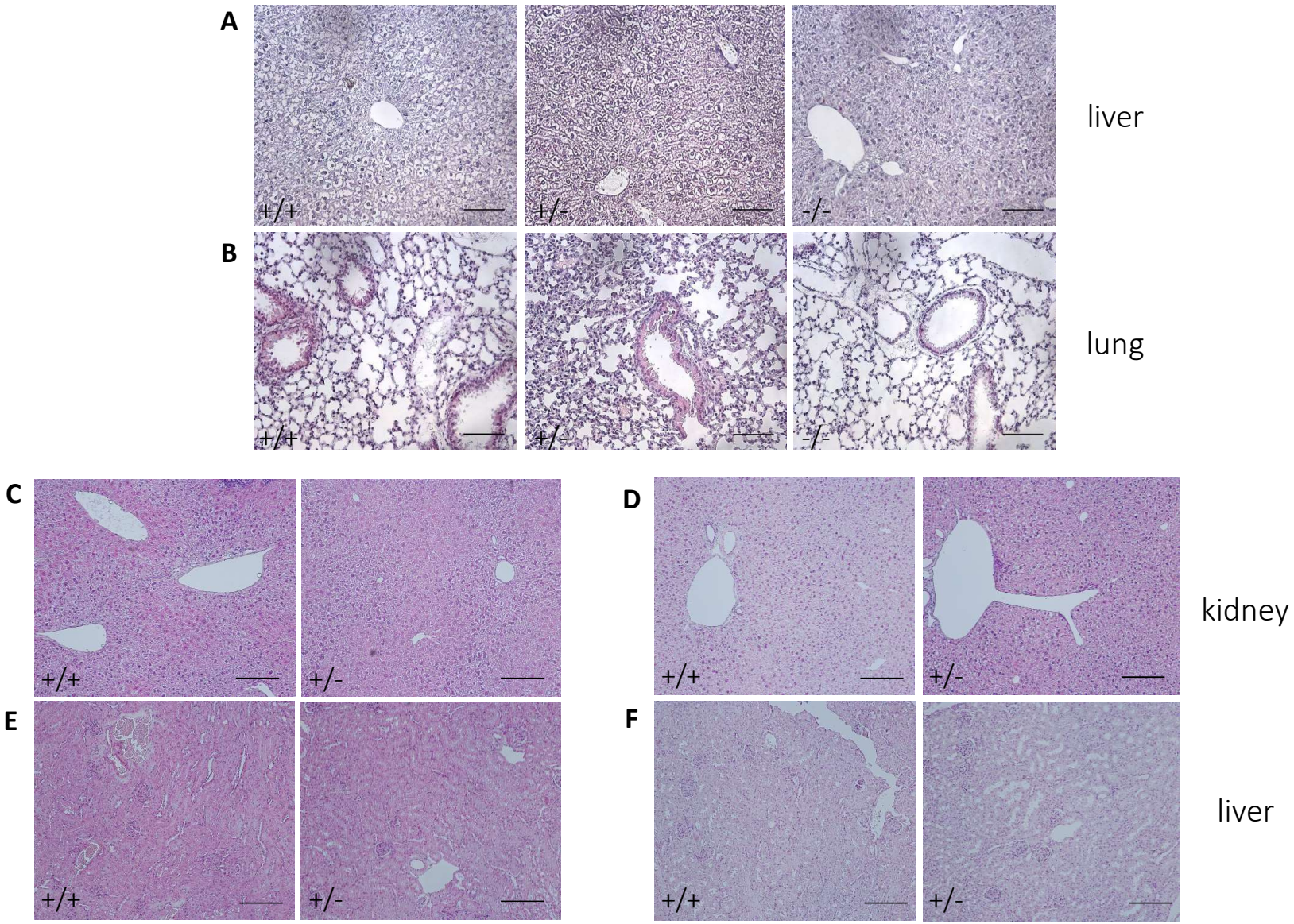

Supplemental Figure 4

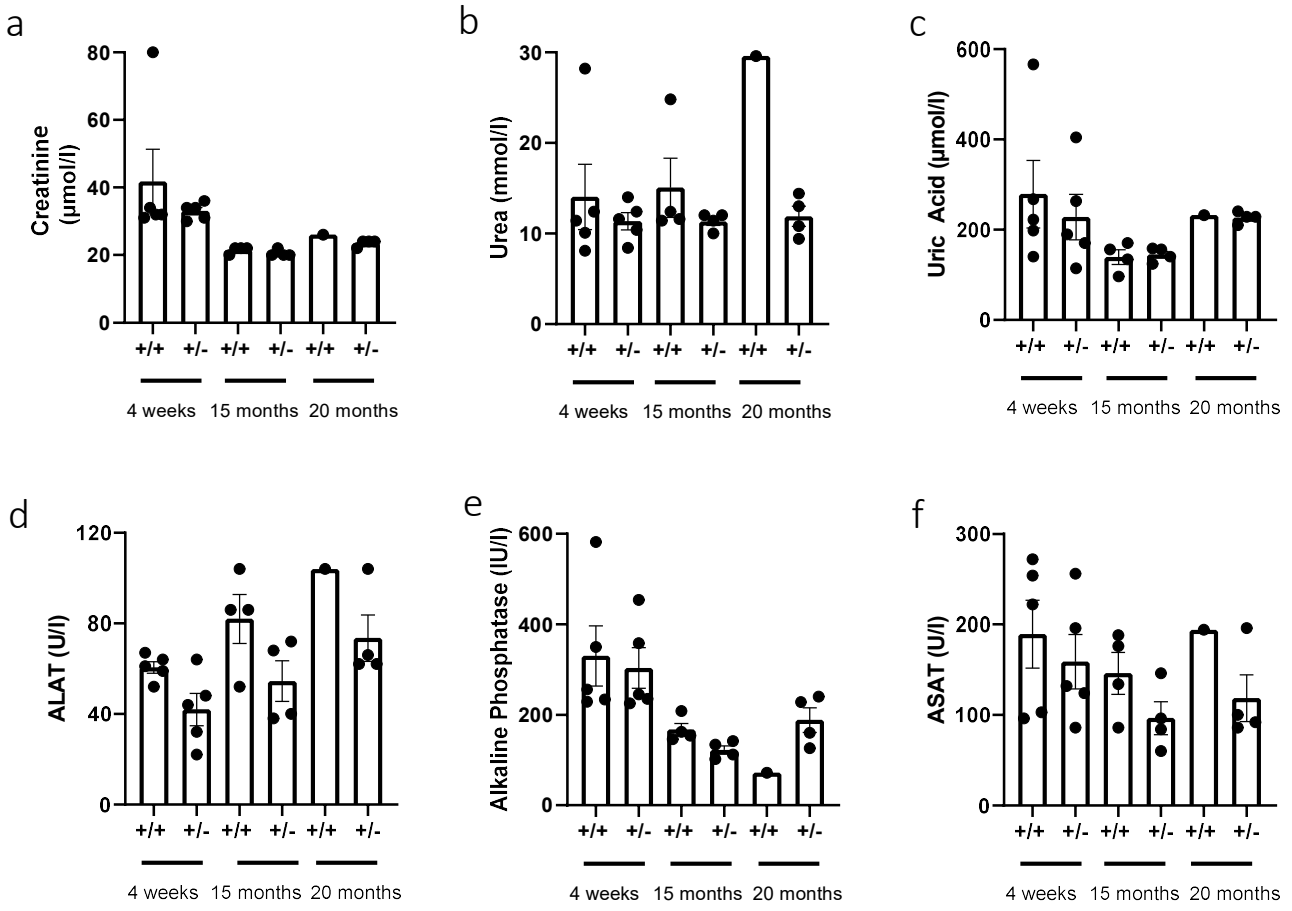

Supplemental Figure 5

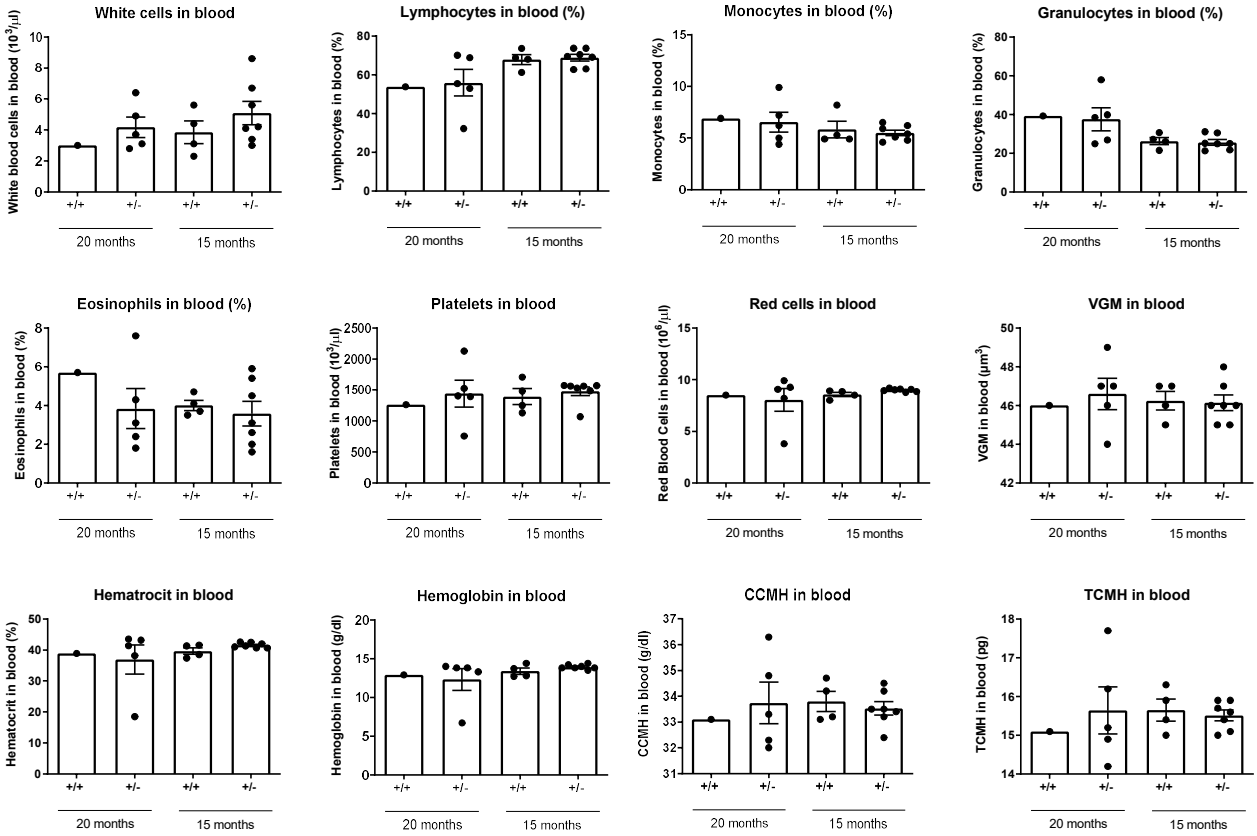

Supplemental Figure 6

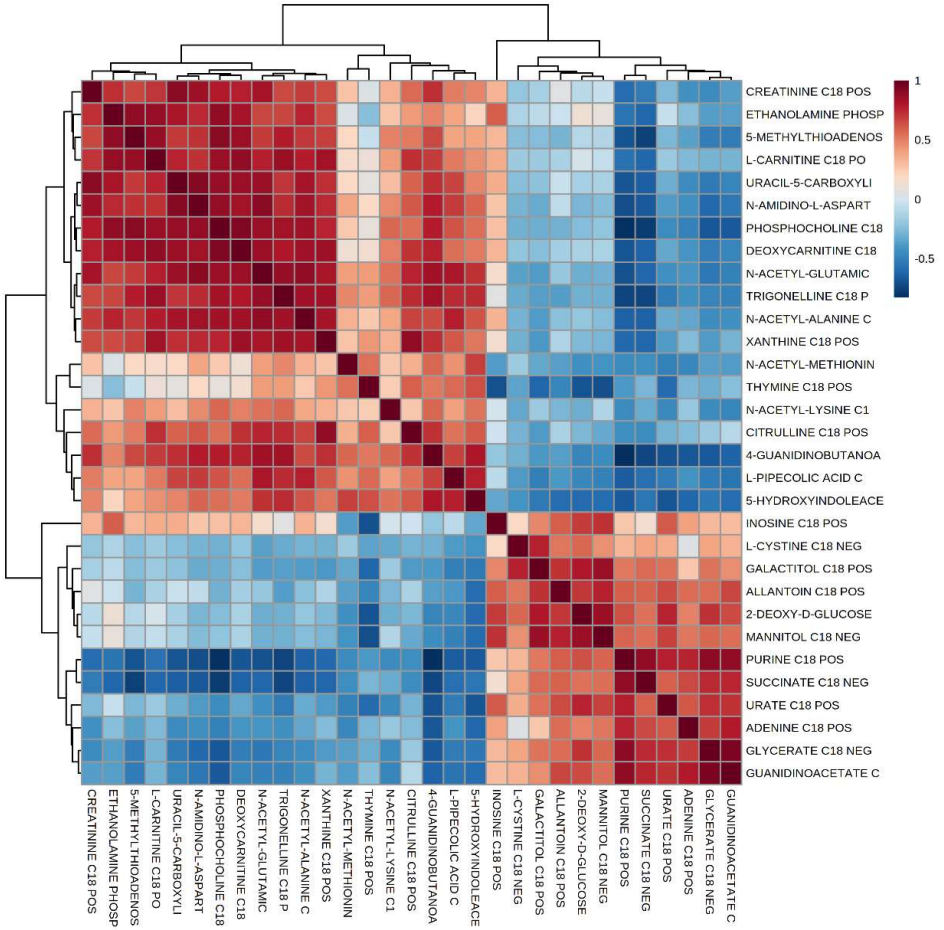

Supplemental Figure 7

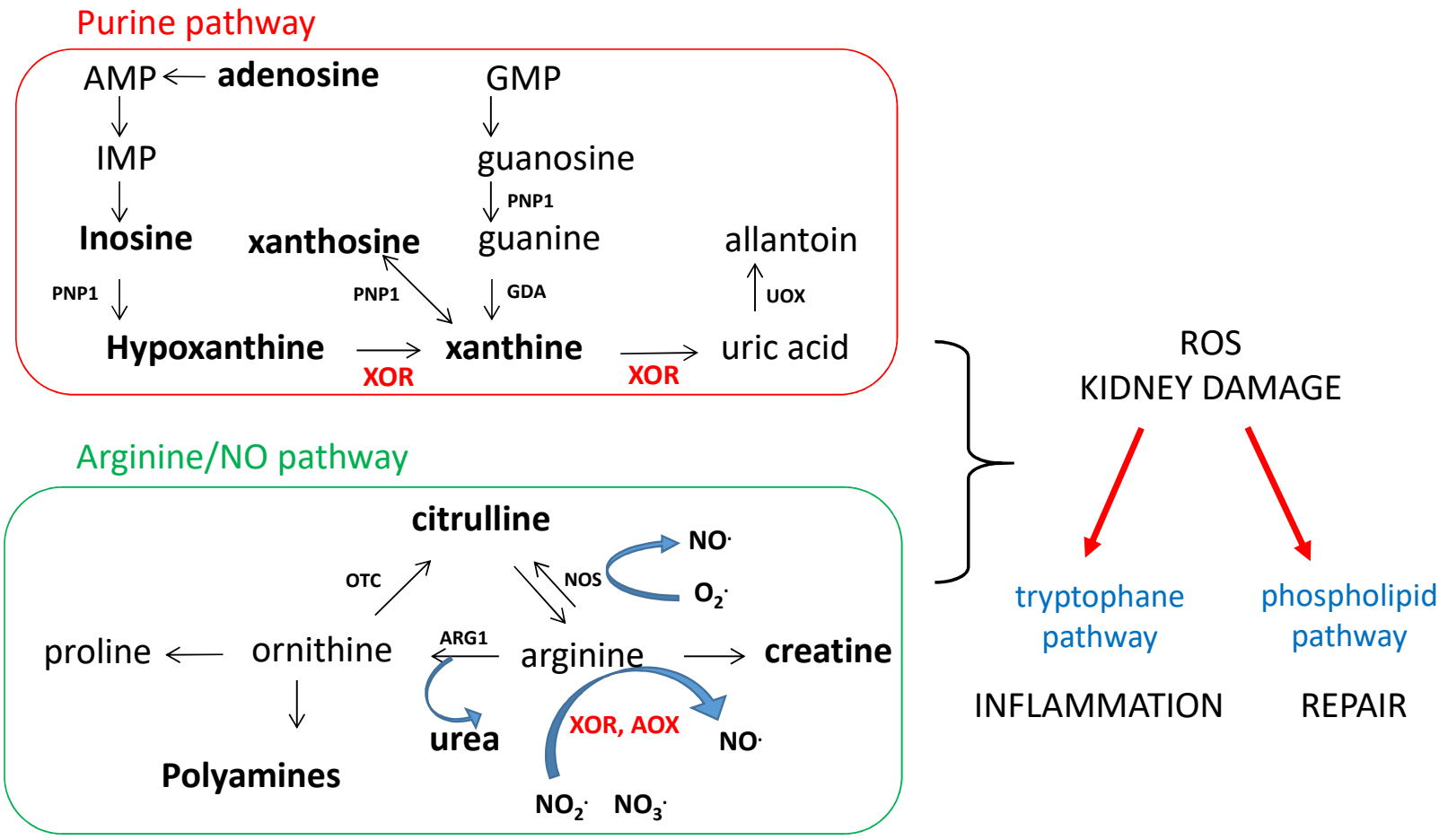

Supplemental Table 1

Mocos	*(F) 5'-CACCACCGCAGAAGACTACAC-3'* *(R) 5'-CACGTTCCGCATACCCACTAC-3'*
TNF-α	*(F) 5'-AAGCCTGTAGCCCACGTCGTA-3'* *(R) 5'-GGCACCACTAGTTGGTTGTCTTTG-3'*
MCP-1/CCL2	*(F) 5'-GCCCCACTCACCTGCTGCTACT-3'* *(R) 5'-CCTGCTGCTGGTGATCCTCTTGT-3'*
Actb	*(F) 5'-TCAGCAAGCAGGAGTACGATGAGT-3'* *(R) 5'-GGGTGTAAAACGCAGCTCAGTAACAG-3'*
Gpx1	QT01195936
Tgfβ	QT00145250
Nox4	QT00126042
Serpine1	QT00154756
Sod1	QT00165039
Tbp	QT00198443
Gclc	QT00130543
Nqo1	QT00094367
Txn1	QT01060297
Txnip	QT00296513
Txndc12	QT00141834

Akr1b8	QT00107800
Cebpb	QT00320313
Pparg	QT00100296

Supplemental Table 2

	$^{+/+}$ vs $^{+/-}$	$^{+/+}$ vs $^{-/-}$	$^{+/-}$ vs $^{-/-}$	$^{+/+}$ vs $^{+/-}$ vs $^{-/-}$
OPLS-DA CV-ANOVA	0.15	9e-012	1e-010	0.12
Metabolite				
1-OLEOYL-GLYCEROL		*		
2-DEOXY-D-GLUCOSE		*		*
4-AMINOBUTANOATE		*		
4-GUANIDINOBUTANOATE		*√	*√	
5-HYDROXYINDOLEACETATE		*√	*√	
5-HYDROXYLYSINE			*	
5-METHYLTHIOADENOSINE		*	*√	*
ADENINE		*	*	*
ALLANTOIN		*√	*√	*
ALPHA-AMINOADIPATE		*		
CITRULLINE		*	*	*
CREATININE		*	*	*
DEOXYCARNITINE		*√	*	*
ETHANOLAMINE PHOSPHATE		*	*	*
ETHYLMALONIC ACID		*		
FORMYL-L-METHIONYL PEPTIDE		*		
GALACTITOL		*	*√	*
GLYCERATE		*	*√	*
GUANIDINOACETATE		*	*√	*
INOSINE		*		*
L-CARNITINE		*	*	*
L-CYSTEIC ACID		*		
L-CYSTINE		*		*
L-PIPECOLIC ACID		*	*√	
MALATE		*		
MANNITOL		*√	*√	*
N-ACETYL-ALANINE		*	*	*
N-ACETYL-GLUTAMIC ACID		*√	*	*
N-ACETYL-LYSINE		*		*
N-ACETYL-METHIONINE		*√		*
N-AMIDINO-ASPARTATE		*	*√	*
NICOTINAMIDE MONONUCLEOTIDE		*		
PANTOTHENIC ACID		*	√	
PHOSPHOCHOLINE		*√	*√	*
PURINE		*√	*√	*
SUCCINATE		*√	*√	*
THYMINE		*		*
TRIGONELLINE		*√	*√	*

URACIL-5-CARBOXYLIC ACID		*	*√	*
URATE		*√	*√	*
XANTHINE		*		*

Listing of discriminant metabolites obtained after univariate analysis [Wilcoxon rank-sum test with an FDR adjusted p-value of 0.05, visualized by *) cumulated with VIP discriminant metabolites obtained after OPLS-DA (visualized by √), CV-ANOVA of the model was given in the first row of the table] from kidney tissues analysis of wildtype, *Mocos*$^{+/-}$ and KO mice.